

UNIVERSIDAD AUTÓNOMA DE MADRID (UAM)
DEPARTAMENTO DE FÍSICA TEÓRICA

**Electron Energy Reconstruction in the
ATLAS Electromagnetic End-Cap
Calorimeter using Calibration Hits**

D.E.A: Eduardo Nebot del Busto
Supervisor: Dr. Jose Del Peso Malagón

Contents

1	Introduction	5
2	The ATLAS detector	7
2.1	The Large Hadron Collider	7
2.2	The ATLAS detector	7
3	Review of calorimetry	13
3.1	Sampling calorimeters	13
3.2	Electromagnetic showers	14
3.2.1	Shower generation	14
3.2.2	Energy resolution	17
4	The ATLAS EMEC	21
4.1	Introduction and Calorimeter requirements	21
4.2	The EndCap Electromagnetic Calorimeter.	22
4.3	Spatial granularity	25
4.4	High Voltage	27
4.5	Presampler	29
5	The Calibration Hits method	31
5.1	Cluster Energy	31
5.2	Description of the method	33
5.3	Corrections for energy depositions in the calorimeter	34
5.4	Correction for lateral leakage out of the cluster	37
5.5	Corrections for longitudinal leakage	39
5.6	Corrections for the energy loss in front of the Calorimeter	41
5.6.1	Region with presampler $\eta < 1.8$	41
5.7	Region without presampler $\eta > 1.8$	44
5.8	Summary	50
6	Results	53
6.1	Energy resolution and linearity	53
6.1.1	Linearity	53
6.1.2	Energy resolution	56
6.1.3	Uniformity of the response	58
6.2	Contribution from the different corrections	59

6.3	Systematics	63
6.3.1	Effect of the cross talk	63
6.3.2	Effect of an imperfect knowledge of the death material	66
6.4	Front method vs X method	70
7	Conclusions	71

Agradecimientos

Me gustaria aprovechar esta oportunidad para dar mi mas sincero agradecimiento a todas las personas que me han estado apoyando durante mi formación.

En primer lugar quiero agradecer a Jose del Peso por haberme acogido como su estudiante y por todo el conocimiento que me ha permitido adquirir el estar bajo su supervisión. El trabajo que se presenta aqui, asi como muchas otras tareas, no hubiesen sido posibles sin su orientacion, comentarios y entusiasmo por mejorar.

Mi presencia en el grupo de altas energías se la debo también a Fernando Barreiro. Le quiero agradecer el interés que ha mostrado tanto por mi trabajo, en el que ha contribuido compartiendo sus conocimientos, como por mi bienestar en todo momento.

A Luis Labarga, primera persona que conocí en la Universidad Autónoma, le tengo que agradecer su acogida y el tiempo que me ha dedicado siempre que he solicitado su ayuda.

No quiero olvidarme de agracer al resto del grupo: Juanjo, Juan, Claudia, Mara, Theodota, Luis Fernando, Pablo y Pachi, que siempre estan dispuestos a echar una mano en lo que se necesite. Y a los que se marcharon: Matti y Conchi.

Por supuesto a todos mis viejos amigos, compañeros de carrera y de doctorado con los que he pasado muy buenos momentos y que siempre me han empujado a seguir adelante. En especial a Carolina, que ha sido compañera de licenciatura, de doctorado y con la que he estado trabajando codo con codo durante los dos últimos años. Ella siempre ha estado ahí para mi y se que segirá estando si la necesito. Y a los nuevos amigos, en especial a Gabe, que ha sido un gran apoyo en los momentos diffiles.

Dejo para el final lo que pienso ha sido mas importante en mi formación como físico y como persona, mi familia. Ellos siempre han estado a mi lado e incluso ahora, separados por unos cuantos miles de kilómetros, todavía siento su apoyo como si estuviesen conmigo. Nunca estaré lo suficientemente agradecido a mis padres por haber tenido una vida de sacrificio para que yo haya podido llegar hasta aquí. En muchas ocasiones he escuchado a personas decir lo orgullosas que están de sus hijos. Pues yo lo estoy de mis padres y por eso esta trabajo va dedicado a ellos.

Chapter 1

Introduction

The Large Hadron Collider, the most powerful proton-proton collider existing so far, it is being installed at CERN (Conseil Européen pour la Recherche Nucléaire) and will start running summer 2008.

The high center of mass energy, high luminosity and several physics channels present at the LHC put several requirements in the expected performance of the ATLAS detector.

The Liquid Argon Electromagnetic End-cap Calorimeter (EMEC), which is basically used to identify and measure the energy and direction of electrons and photons, will be very important on the LHC since many of the physics events have electrons and photons in their final states. The LAr Calorimeter has been mounted and commissioned since last year in the ATLAS cavern and some problems have been encountered and solved already. Furthermore, previous tests with electron beams of known energy showed that the different calorimeter requirements were fulfilled for the few modules tested (3 out of 16 modules for the EMEC). However, the nominal ATLAS set-up it is different compared to the one at the beam tests. Electrons and photons coming from the interaction point will go through the inner detector, cables, boards, cryostat walls, etc, before reaching the electromagnetic calorimeter. In addition, they will feel the effect of a 2 Tesla magnetic field, which may bend the trajectory, specially of the low energetic electrons, making miss the calorimeter cell cluster. These conditions in ATLAS will affect the energy reconstructed in the calorimeter for incident electrons and photons as well as the energy resolution with respect to the Beam Tests. The correction for this energy loss was done in the past using some weighting procedure in the different calorimeter compartments. It was shown that this procedure was not satisfactory to reconstruct the energy at the level required.

A new method to reconstruct the energy of electrons and photons, called Calibration Hits Method (CHM), was devised almost two years ago and has been developed and tested for the Electromagnetic Barrel calorimeter (EMB) thereafter [12]. Simultaneously, the author of this "tesina" has adapted and tested the method for the Electromagnetic End-Cap Calorimeter (EMEC) and perform some further developments to the method demanded by some peculiarities of the EMEC. This is the work done in this "tesina".

The Calibration Hits Method is named after a special Monte Carlo simulation which records not only the energy depositions in the active parts of the calorimeter but also in the inactive parts and dead materials. This allows to compute correction functions for all the different sources of energy loss independently. The parameters of these functions depend on the following measurable quantities: the energies deposited in the 3 calorimeter compartments and in the presampler, and both the barycenter in depth and along the direction of the polar angle. The simulation of the electron samples to develop the method and extract the coefficients require a large CPU time, so the grid computing facility at the UAM high energy physics laboratory was used.

Chapter 2 will give an overview of the LHC and ATLAS detector. Chapter 3 introduces the basics of electromagnetic calorimetry paying special attention to sampling calorimeters. In Chapter 4 a description of the Endcap electromagnetic Calorimeter is given, with emphasis in the topics of interest for this work. In Chapter 5 a description of the Calibration Hits method and the work to obtain the different corrections is presented. Finally, Chapter 5 presents the achieved results by the method in terms of energy resolution, energy scale and linearity, and some systematic errors are studied.

Chapter 2

The ATLAS detector

In this chapter the motivation and the main characteristics of the Large Hadron Collider (LHC) as well as the ATLAS detector are discussed. In the first section the most important accelerator parameters are reviewed. In the second section a brief overview of the ATLAS detector is done.

2.1 The Large Hadron Collider

The LHC is a proton-proton and heavy ion collider with a center of mass energy of 14 TeV when operating in p-p mode. The accelerator, being mounted in the $\sim 26.7\text{Km}$ circular LEP tunnel, is currently on the last installation stages: the first proton-proton collisions are expected in summer 2008. The accelerator is basically formed by 1232 superconducting dipoles, providing a magnetic field of 8.4T which will keep the protons circulating. Bunches of protons separated by 25ns will intersect at the four interaction points where the four different detectors (ATLAS, ALICE, CMS and LHCb) are placed, figure (2.1). ATLAS and CMS are general purpose experiments designed for searches of new physics and precision measurements; LHCb is a B physics oriented detector while ALICE is a heavy ion experiment trying to study the behavior of nuclear matter at very large energies.

In the first LHC runs a luminosity of $2 \times 10^{33}\text{cm}^{-2}\text{s}^{-1}$ is expected, which will be increased afterwards to its nominal value of $10^{34}\text{cm}^{-2}\text{s}^{-1}$ equivalent to an integrated luminosity of 100fb^{-1} a year. The design of the LHC makes it possible to explore an unprecedented physical region, where new physics phenomena may appear.

2.2 The ATLAS detector

The ATLAS (A Toroidal Apparatus) is a multi-purpose detector designed to exploit the physics potential of the LHC. The detector, figure 2.2, is a cylinder 44 meter long, 11 meters radius and an overall weight of 7000 tons [1]. The ATLAS coordinate system is a spherical system defined in terms of the beam direction, which is the z axis, and the polar (θ) and azimuthal (ϕ) angle. However, the polar coordinate it is usually expressed in terms of the pseudo-rapidity which is defined as:

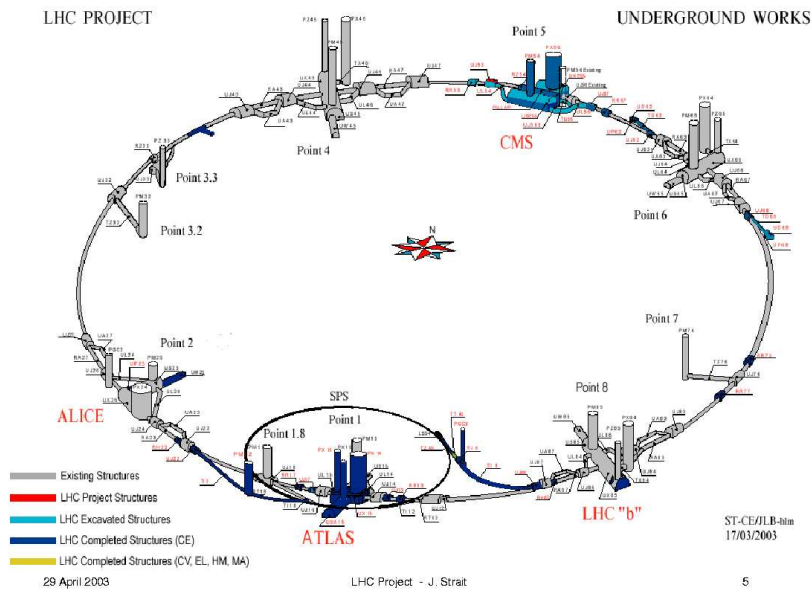


Figure 2.1: Diagram of LHC ring.

$$\eta = -\ln\left(\tan\left(\frac{\theta}{2}\right)\right)$$

The detector is made of four major components:

- The Inner detector (ID). It is a tracking detector located in the most inner part of ATLAS, which is enclosed within a cylinder that has a length of $7m$ and a radius of $1.15m$ (see figure 2.3). It is designed to measure the trajectory (track) of charged particles with a very good efficiency in the coverage range $-2.5 < \eta < 2.5$. It is immersed in an axial magnetic field of $2 T$ for the measurement of the momentum of charged particles. It consists, from inner to outer volume, of three parts: two types of Silicon semiconductor (Pixel and SCT) and straw-tube tracking detectors (TRT). The combination of Pixel and SCT allows for the reconstruction of particle decay length for unstable particles, while the TRT implements an identification of electrons through the transition radiation effect. Some of the measurements which can be performed using the ID signals are: identification of the primary vertex or interaction point, determination of the trajectory and momentum of charged particles, decay length reconstruction, electron identification and measurement of charge sign.
- The Calorimeters. The system of calorimeters can be seen in figure 2.4.
 - The Electromagnetic (EM) Calorimeter is used to identify electrons and photons, and to measure their energy and direction. It is also part of the hadronic calorimeter when measuring the energy of jets and the missing

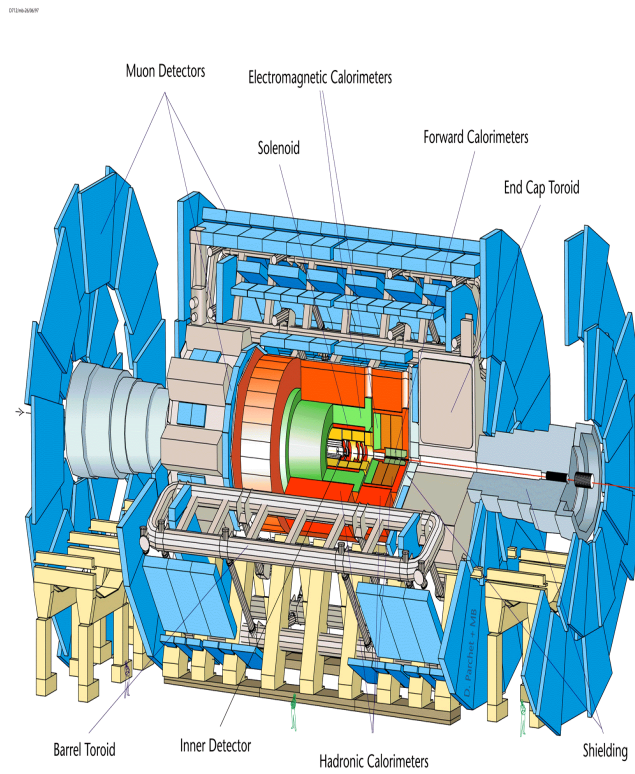


Figure 2.2: View of the atlas detector.

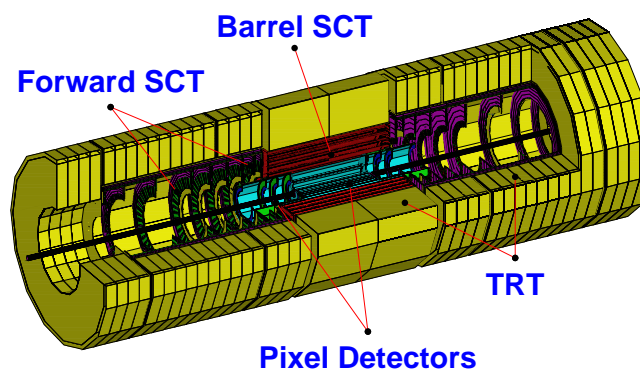


Figure 2.3: View of the Inner detector.

transverse energy (E_T^{miss}) of some processes. The EM calorimeter is a lead - liquid Argon sampling calorimeter with fine granular cells, which covers a pseudo-rapidity range $-3.2 < \eta < 3.2$ and the whole range along the azimuthal (ϕ) direction. It is divided in one barrel ($-1.475 < \eta < 1.475$) and two end-caps ($-3.2 < \eta < -1.375$, $1.375 < \eta < 3.2$) [2].

- The hadronic Calorimeter will be used to measure the energy of jets and missing transverse energy (E_T^{miss}). It is divided in one barrel and two End-Caps. The barrel part is a sampling iron - scintillator calorimeter readout by optical fibers and photo-multipliers. The scintillator pieces are placed normal to beam axis like "tiles", hence the name of Tile Calorimeter. The End-Caps are sampling calorimeters with copper as absorber and liquid Argon as sensitive material which share the cryostats with the EM End-Cap and forward calorimeters.
- The forward calorimeter is realized to achieve a good hermeticity in ATLAS, hence to provide an excellent resolution in the measurement of missing transverse energy. It covers the region in pseudo-rapidity $-4.9 < \eta < -3.2$ and $3.2 < \eta < 4.9$. It is a sampling calorimeter, with liquid Argon as sensitive material, segmented longitudinally in three compartments: FCAL1, FCAL2 and FCAL3. As absorber material the first one uses copper while the last two use tungsten inside copper tubes.

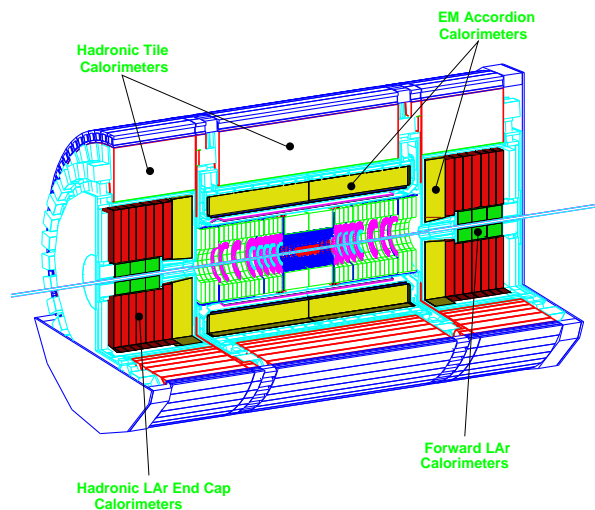


Figure 2.4: Schematic view of the ATLAS calorimeters.

- The muon spectrometer. It is a tracking detector for precise measurements of muon trajectory and transverse momentum. It consists of gas proportional

chambers which surrounds the calorimeter and are immersed in a magnetic field, with maximum value of $4 T$, for the measurement of the muon transverse momentum. There two types of chambers: MDT in the barrel location and CSC in the End-Caps. Additionally there are fast response chambers to trigger on muons, which are called RPC in the barrel region and TGC in the End-Caps. Both chamber types for trigger purposes are capable of delivering the response in a short time, between 15 ns and 20 ns , shorter than the crossing time of LHC beam proton bunches. The chambers extend to the ATLAS dimensions, for the barrel part to a radius of 11 m and for the the End-Caps to a length of 23 m from the nominal interaction point.

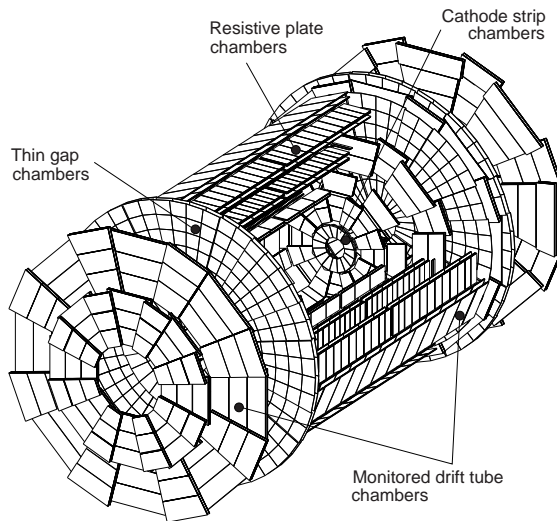


Figure 2.5: View of the muon system.

- The magnet system. The ATLAS superconducting magnet system consists of a central solenoid providing the magnetic field for the Inner Detector and a system of large air-core toroids generating the magnetic field for the muon spectrometer.

The solenoid magnet is place just in front of the Barrel Electromagnetic Calorimeter and it is cooled by helium at 4.5 K . It provides a magnetic field along the z -direction of about $2 T$. As a drawback it increases the material in front of the EM Calorimeter causing electrons and photons showering before they reach the active part of the calorimeter.

The toroid magnet is divided into one barrel part and two End-Caps. Both are visible in the outer part of the ATLAS detector (figure 2.2).

Chapter 3

Review of calorimetry

In this chapter an overview of the principles of calorimetry in high energy physics is given. First the concept of *sampling calorimeter* will be explained and then the *electromagnetic particle showers or cascades*.

3.1 Sampling calorimeters

Calorimeters currently used in high energy physics are either *homogeneous* or *sampling*. Homogeneous calorimeters consist of a single material, such as lead glass, NaI, BGO, etc... When a fast particle enters the acceptance volume of a homogeneous calorimeter its energy degrades and generates a measurable signal. On the contrary, the tasks of absorbing the incident energy and generating a signal are, in sampling calorimeters, done by two different materials: the *passive* material (Fe, Cu, Pb, U, etc...) plays the role of energy absorber, whereas the *active* material (scintillating plastic, LAr, silicon) gives rise to the signal. This work is focused on sampling calorimeters.

The two materials present in a sampling calorimeter are typically arranged in successive layers, so that the incident particle and the secondary ones generated by its interaction with the detector, cross alternatively regions of active and passive material as they go deeper and deeper into the detector. The interaction just mentioned usually produces a so called *shower* or *cascade* of secondary particles in which the energy carried is degraded and part of it detected. Particle showers will be described in 3.2.

The principles of the shower generation are of statistical nature. Therefore the fraction of energy that an incident particle leaves inside the active medium can be regarded as a random variable, subject to fluctuations. The geometry of a calorimeter can be very complicated. For the sake of simplicity one can consider the simplest plane-parallel layered structure as an example. In any case, the signal generated by an incident particle must be, on average, proportional to its original energy.

In order to gain some insight into the features of the energy signals generated in a sampling calorimeter, it is necessary to describe particle showers.

3.2 Electromagnetic showers

We call electromagnetic showers to those generated by an electron, positron or photon reaching a calorimeter. In this paragraph the mechanism of shower generation and the resolution achievable in an energy measurement involving an electromagnetic shower are discussed.

3.2.1 Shower generation

Several mechanisms contribute to the energy loss of electrons and photons incident on matter. However at high energies (well above 10 MeV) the fraction of energy lost per unit depth of material is almost energy independent and only due to bremsstrahlung (electrons or positrons) and pair creation (photons). The secondary particles produced in the cascade carry successively less energy until they reach the range where several other effects become important. If the whole shower is absorbed inside the calorimeter, the energy deposited is obviously equal to that of the primary particle.

For electrons and positrons the processes that become relevant in the sub- GeV range are Bhabha and Compton scattering and ionization. Positrons in addition suffer annihilation. Ionization is in fact the dominant process and the reason why all particles finally get absorbed. For photons the Compton and photoelectric effect are the ones that compete with pair production at low energies.

At high energies ($E > 1\text{ GeV}$) the absorption can thus be characterised in a material-independent way by introducing the so called *radiation length* (X_0) of the substance. It is defined as the material thickness to be travelled by an electron so that it loses on average 63.2% of its energy through bremsstrahlung; i.e. the electron energy decreases by a factor $1/e$ each radiation length. This obviously means that the typical shower particle energy at a given depth z (given in cm) is

$$E = E_0 \cdot e^{-\frac{z}{X_0}} = E_0 \cdot e^{-t}$$

where E_0 is the initial energy of the incident electron or positron. Obviously t is the depth measured in units of X_0 .

At low energies, energy losses are dominated by collisions. The *critical energy* ϵ_0 of a material is the energy value at which the mechanisms of bremsstrahlung and ionization are equally important. It represents the limit where the growth of the shower stops and the particle multiplicity starts to decrease. Its value in MeV is given approximately by [3]:

$$\epsilon_0 = \frac{550}{Z}$$

This approximation is accurate to 10% for an atomic number $Z > 13$.

A very simplified model of shower development can provide some insight into electromagnetic calorimetry, assuming that the only dominant processes at high energies are bremsstrahlung and pair production and describing these two mechanisms by asymptotic formulae.

An electron entering a calorimeter with energy E much larger than the critical energy ϵ_0 , after having crossed one radiation length of material (X_0), will have lost 63% of its initial energy into photon. We can say that on average the photon and the electron will carry each half of the original energy, $E/2$. After another radiation length of material the photon will create an e^+e^- pair and the electron will emit another bremsstrahlung photon. The energy of each of the four particles will be on average $E/4$. The multiplication process proceeds. When the shower particles reach an energy below ϵ_0 they are completely absorbed by collisions and the shower terminates. The model is equally valid if the original particle is a photon, except for a small shift in depth.

The number of particles doubles after each radiation length. Therefore at a depth t (in units of X_0) the number of shower particles is

$$N = 2^t$$

The mean energy of a particle will then be

$$\epsilon = \frac{E}{N} = E \cdot 2^{-t}$$

The depth at which the mean energy ϵ equals the critical energy ϵ_0 is where the shower reaches its maximum particle multiplicity, that is:

$$\ln(N_{max}) = \ln(E/\epsilon_0) \Rightarrow \ln(2^{t_{max}}) = \ln(E/\epsilon_0)$$

Hence,

$$t_{max} \simeq \frac{\ln(E/\epsilon_0)}{\ln 2} \quad (3.1)$$

The average total distance covered by all the particles of the shower is called the average *total track length* T . Since each particle travels on average a distance X_0 before splitting into two, the quantity T , in units of X_0 , is equal to the total number of particles in the shower.

As the showering process occurs, a small part of the energy is lost by ionization and this fraction is proportional to the total track length, because each energetic particle of the shower deposits an amount of energy per unit length independent of the energy it carries. That is:

$$E_{visible} = E_{ionization} \propto T = \frac{E}{\epsilon_0}$$

This linear relation between the incident energy and the total track length or energy loss by ionization makes calorimeters useful devices.

In general the whole track length will not be detectable, but only a fraction of it, T_d . Only shower particles above a certain energy threshold η will be detected, so we can write

$$T_d \simeq F(\eta) \cdot T = F(\eta) \cdot \frac{E}{\epsilon_0}$$

In order to ensure the full containment of the shower in the calorimeter, both experimental information and some calculation can be used [4]. The length necessary to ensure a 98% energy shower containment can be parametrized as

$$\langle L_{98\%} \rangle \simeq t_{max} + 4\lambda_{att}$$

where the quantity λ_{att} comes from the exponential decay of the shower energy density deposition (following $e^{-t/\lambda_{att}}$) after reaching the maximum (see 3.1). This λ_{att} turns out to be approximately energy-independent and can be characterized in terms of the radiation length as $\lambda_{att} \simeq (3.4 \pm 0.5)X_0$. Notice that the depth necessary for a calorimeter to fully contain and measure a shower grows only *logarithmically* with the energy (see eq. 3.1).

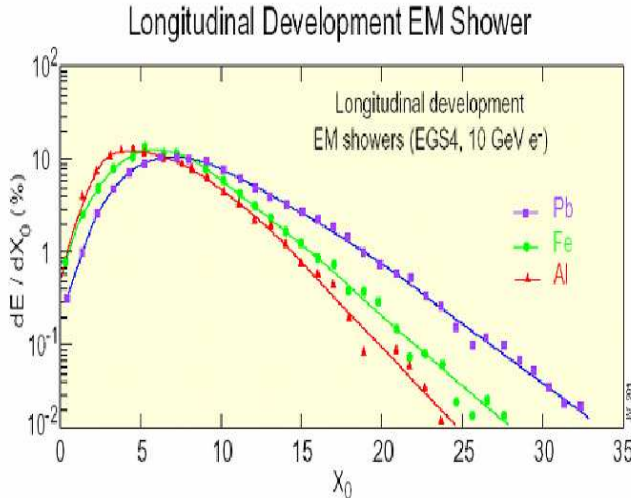


Figure 3.1: Average longitudinal energy deposition of electromagnetic showers for three types of materials: Lead (blue), Iron (green) and Aluminum (red).

The shower also develops transversally to the primary particle direction due to the scattering angle of the different interaction processes. Averaging to enough number of events, the transverse energy deposits of the shower can be parametrized by two decreasing exponential functions in the polar variable r , with different length parameters [5]. The first exponential with a small mean length represents the core of the shower, while the second one with a larger mean-length takes into account the spread of the low energy particles in the last stages of the shower development (mainly the multiple scattering process). The fluctuations around this average transverse profile are estimated to be small. The Molière radius (R_M) is a characteristic constant of a material giving the scale of the transverse dimension of the shower in units of radiation lengths. By definition, a cylinder with axis the direction of the incident electron and radius $2R_M$ contains on average 95% of the shower energy. An approximate relation for R_M is:

$$R_M = 0.0265X_0(Z + 1.2)$$

For example, for lead $R_M = 12.3 \text{ mm}$ and for liquid Argon $R_M = 71.2 \text{ mm}$.

3.2.2 Energy resolution

The processes of energy deposition, detection and read out are of statistical nature. The relative precision of the energy measurement can be obtained as:

$$\frac{\sigma(E_{visible})}{E_{visible}}$$

where $\sigma(E_{visible})$ is the standard deviation of the variable $E_{visible}$.

Intrinsic fluctuations

Two kinds of uncertainties enter the energy measurement. First, the showering is in itself a statistical process, of almost gaussian character. Landau fluctuations [6] due to ionization processes with large energy transfer to the electrons of the detector material, lead to asymmetric spectra. They are however not quantitatively significant in the case of the ATLAS calorimeter.

The visible energy is, as shown above, proportional to the number of particles produced (N), but also to the number detected (N_d). Both are large numbers that will follow normal distributions. The standard deviation will thus scale as $\sigma \sim \sqrt{N}$. Then

$$\frac{\sigma(E)}{E} \sim \frac{\sigma(N_d)}{N_d} = \frac{\sqrt{N_d}}{N_d} = \frac{1}{\sqrt{N_d}} \propto \frac{1}{\sqrt{E}}$$

The relation stated above sets a lower limit to the accuracy of the energy measurement, i.e. the *intrinsic fluctuations*. The best homogeneous calorimeters made of scintillating crystals or noble liquids achieve energy resolutions of order $\sigma/E \simeq 1\%/\sqrt{E}$ [4].

Sampling fluctuations

In the case of a sampling calorimeter only the fraction of the particle track that is inside the active part will contribute to the visible signal. Hence, we need to decrease T_d by a factor to consider only the active part. However, we will follow in this section an alternative approach, which uses the sampled (or visible) energy instead, Let E_s be the sampled energy, s the thickness of one calorimeter active layer and $(dE/dx)_s$ the energy deposited by minimum ionising particles in the active layers per unit length. Hence, the number of crossing through the active medium layers will be:

$$N_s = \frac{E_s}{(dE/dx)_s s}$$

The visible energy can approximately be computed as:

$$\frac{E_s}{E} \sim \frac{\left(\frac{dE}{dx}\right)_s s}{\left(\frac{dE}{dx}\right)_s s + \left(\frac{dE}{dx}\right)_d d}$$

where d is the thickness of the absorber layers, and both s and d are expressed in units of radiation lengths.

Since normally $(\frac{dE}{dx})_d d \gg (\frac{dE}{dx})_s s$, we can write the following approximation:

$$\frac{E_s}{E} \sim \frac{(\frac{dE}{dx})_s s}{(\frac{dE}{dx})_d d}$$

Hence,

$$N_s \sim \frac{E}{(\frac{dE}{dx})_d d}$$

Therefore,

$$\frac{\sigma_s}{E_s} = \frac{1}{\sqrt{N_s}} = \sqrt{\frac{(\frac{dE}{dx})_d d}{E}}$$

If d is in units of X_0 :

$$\left(\frac{dE}{dx}\right)_d \sim \frac{E}{T} = \epsilon_0$$

where ϵ_0 is the critical energy of the absorber material, then,

$$\frac{\sigma_s}{E_s} = \sqrt{\frac{\epsilon_0 d}{E}}$$

where d is given in units of X_0 .

Expressing the critical energy ϵ_0 in units of MeV and the energy E in GeV , previous relation becomes:

$$\frac{\sigma_s}{E_s} = 0.032 \sqrt{\frac{\epsilon_0 d}{E}} = R \sqrt{\frac{d}{E}}$$

where $R = 0.032\sqrt{\epsilon_0}$.

The formula above must be corrected for multiple scattering. Once the passive material is fixed, this correction can be reabsorbed in the constant R . The sampling fluctuations of the ATLAS Electromagnetic Calorimeter followed the previous approach, hence, the decrease law as $1/\sqrt{E}$.

Other fluctuations.

There are other sources of degradation of the energy resolution like non-uniformities, mechanical imperfections, energy leaking behind the calorimeter (in case the depth is not enough), misscalibrations, etc.

In general this type of imperfections do not follow the same scaling law as the sampling fluctuations, generating a constant term that dominates the energy resolution at high energies.

To sum up, the energy resolution of a sampling calorimeter can be parametrized by the formula ¹

$$\frac{\sigma_E}{E} = \frac{a}{\sqrt{E}} \oplus b$$

where the symbol \oplus stands for the quadratic sum, that is:

$$\frac{\sigma_E}{E} = \sqrt{\frac{a^2}{E} + b^2}$$

The presence of noise, for instance in the readout chain, introduces an additional term which scales as $1/E$, since the $\sigma(\text{noise})$ does not depend on the energy of the incoming particle. Hence,

$$\frac{\sigma_E}{E} = \frac{a}{\sqrt{E}} \oplus b \oplus \frac{c}{E}$$

¹Electronics noise is not taken into account at this stage.

Chapter 4

The ATLAS EMEC

4.1 Introduction and Calorimeter requirements

Electromagnetic Calorimetry will play a main role in the understanding of the physics outcoming from proton-proton collisions in the LHC, since many processes will manifest themselves through photonic and electronic final states. The main task of the atlas electromagnetic calorimeter is to measure energy and position of electrons, photons and jets (portion of jets), measurement of the transverse momentum (p_T) of the event and particle identification (specially electrons and photons). It is the only device to identify photons, since they do not leave any track in the Inner Detector. Several benchmark physics channels such as $H \rightarrow \gamma\gamma$, $H \rightarrow 4e$ or Z ' or W ' identification put the most tight constraints on the construction of the calorimeter. In this document we just describe those requirements of interest for the understanding of the presented work:

- Search for rare processes require a very good η coverage, as well as the measurement of the missing transverse energy of the event.
- The strongest constraints in terms of energy resolution are based on higgs searches. The channels $H \rightarrow \gamma\gamma$ and $H \rightarrow 4e$ need a mass resolution of 1% in the region $114\text{GeV} < M_H < 219\text{GeV}$ which requires a sampling term of about $\sim \frac{10\%}{\sqrt{E(\text{GeV})}}$ and a constant term lower than $\sim 0.7\%$. In addition the energy scale must be controlled at the level of 0.1%.
- It is necessary to obtain a linearity better than 0.1%.
- Electron reconstruction capability from 1 GeV to 5 TeV . The lower limit comes from the need of reconstructing electrons from b quark decay. The upper one is set by heavy gauge boson decays.
- The total thickness of at least 24 radiation lengths (X_0) such that the resolution, linearity and energy scale are not affected by energy leaked behind the calorimeter for high energy particles ($E > 500\text{GeV}$).

- Excellent electron/jet and photon/jet separation. The main source of missidentification of electrons and photons is hadronic jets. For example, a high p_T π^0 decays in two high p_T photons, which, going very close together, may look as one photon of a Higgs decay channel $H \rightarrow \gamma\gamma$. To distinguish the two photons of the π^0 decay, a fine lateral (granularity) in the calorimeter is required.

4.2 The EndCap Electromagnetic Calorimeter.

The ATLAS Electromagnetic End-Cap Calorimeter, is a sampling calorimeter with lead as absorber or passive material and Liquid ARgon (LAR) as an active material [2]. An accordion shape is given to all plates in order to avoid crack regions due to cables and boards of the readout. A picture of the accordion shape is shown in figure 4.1. Particles, which are incident onto the calorimeter from left to right of the picture, perceive the alternate Lead-LAR structure of the sampling calorimeter.

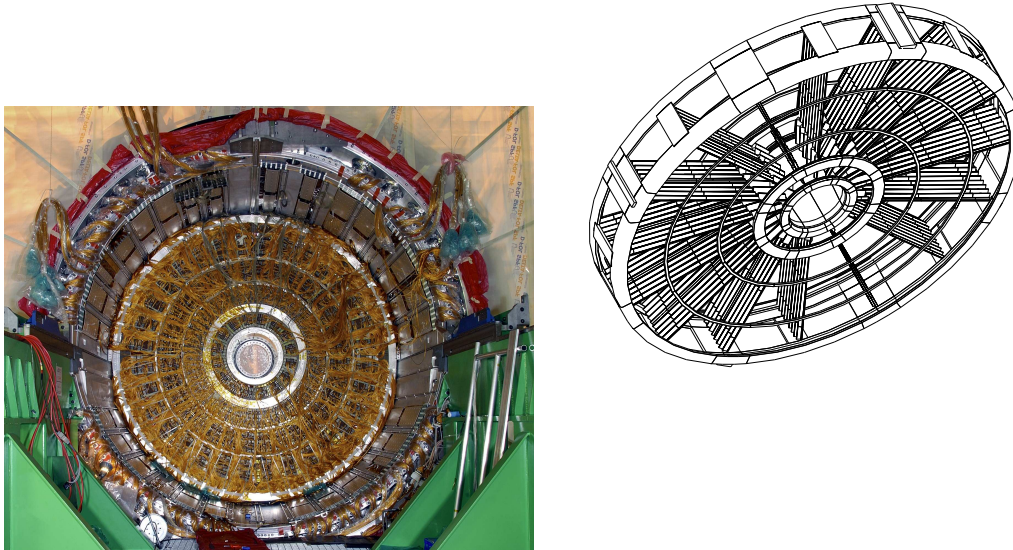


Figure 4.1: Accordion shape in EMEC inner wheel

The Argon is kept liquid at a temperature of $\sim 89^\circ K$ through a cryogenic system, being the EMEC inside a cryostat vessel, which has two walls separated by vacuum for better thermal isolation.

There are two EMEC, in their respective cryostats, located at the two mirror End-Cap positions, one at $z \sim -350$ cm (EMEC-C) and the other one at $z \sim 350$ cm (EMEC-A) of the nominal ATLAS interaction point (see figure 2.2). Each EMEC End-Cap has a cylindrical (wheel) form being the internal and external radii of about 30 cm and 200 cm respectively, and about 63 cm thick. In Figure 4.2 a picture of one EMEC inside the cryostat, seen from the back, is shown, together with a schematic drawing of the EMEC cylinder with some absorbers in it. The readout cables (orange-color) coming from the back side are seen in the picture as well as the 30cm-radius hole in the center to accommodate the beam pipe (as well as to leave place to the forward calorimeter behind). In order to accommodate the accordion

geometry the absorber plates are arranged radially like the spokes of a bicycle wheel and the accordion waves are parallel to the front and back edges of the wheel and run in depth (see drawing of figure 4.2).



(a) Picture of an EMEC wheel inside the End-Cap Cryostat. (b) Arrangement of absorbers in an EMEC cylindrical wheel

Figure 4.2: EMEC figures

Since the EMEC is a cylindrical wheel, the amplitude of the accordion waves decreases when η increases (when the radius decreases).

Due to mechanical constraints demanded by this accordion shape, a second independent wheel is needed to extend the coverage to $\eta = 3.2$. Hence, there are two wheels, the outer wheel from $\eta = 1.375$ to $\eta = 2.5$ and the inner wheel from $\eta = 2.5$ to $\eta = 3.2$. In the picture of figure 4.2 a metal ring is clearly seen separating the two outer and inner wheels, which is shown in the drawing as well. A discontinuity in the accordion wave shape is seen in the drawing of figure 4.2 when going from the outer to the inner wheel, and can be clearly seen in figure 4.3 where a detail picture of the outer-inner boundary is shown.

The lead is clad by 0.2 mm thick steel to give it enough rigidity. For the outer wheel, the thickness of the lead plates is 1.7 mm while the LAR gap thickness between two absorbers decreases continuously from 5.6 mm (at $\eta = 1.375$) to 1.8 mm (at $\eta = 2.5$). For the inner wheel, the thickness of the lead plates is 2.2 mm (see figure 4.3) while the LAR gap thickness between two absorbers decreases continuously from 6.2 mm (at $\eta = 2.5$) to 3.6 mm (at $\eta = 3.2$).

The LAR ionization is collected by electrodes (at high voltage) situated in between two absorbers (at ground) as can be seen in figure 4.3 for the inner wheel as an example. To keep the electrode in the right place, honeycomb spacers are located



Figure 4.3: Stacked layer of the inner wheel. The electrode is placed in between two absorbers.

in between the absorber and the electrode, which are also distinguished in figure 4.3. Hence the liquid Argon gap between two absorbers is divided in two parts, the ionization of both being readout by the same electrode. A picture of an outer-wheel electrode is shown in figure 4.4. In the thickness of $0.25mm$ there are 3 copper layers separated by Kapton isolation, namely two layers on top and bottom holding the High Voltage and one layer in the middle to readout the ionization signal by the effect of capacitance coupling. The thicknesses of these layers are given in figure 4.4. The High Voltage (HV) held on the bottom and top electrode layers ranges between 1000 Volts and 2500 Volts depending on pseudorapidity (η) location. For such high values of the voltage a very good isolator, like Kapton, is mandatory to avoid leak current to the signal layer.

To facilitate handling and logistics each EMEC cylinder is divided into 8 octants or modules (see figure 4.5), hence there are 16 modules in total for the two EMEC End-Caps. One half of the modules have been stacked at the CPPM ¹ and the other half at UAM ² under strict clean conditions. These clean conditions are important to avoid short-circuits due to any dust particle entering in the gap between electrode and absorber where the electric field may be higher than $1000 V/mm$.

One module consists of 96 (32) layers for the outer (inner) wheel stacked one on top of each other along the azimuthal direction (ϕ). Each layer is a sandwich of absorber, spacer (gap), electrode, spacer (gap). Figure 4.5 represents a picture of a module at the stacking frame of the UAM clean room.

The design is symmetrical in ϕ .

¹Centre de Physique des Particules de Marseille

²Universidad Autónoma de Madrid

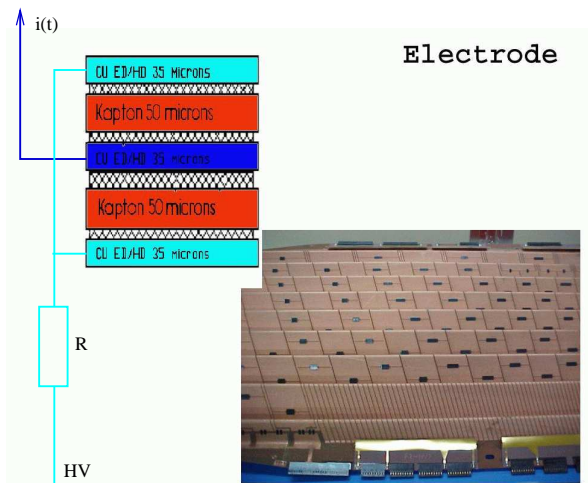


Figure 4.4: Picture of an EMEC electrode. The thin electrode has 3 layers separated by Kapton isolation: two HV layers on the sides and one signal layer inbetween which capture the ionization signal by capacitance coupling.

4.3 Spatial granularity

The EMEC is segmented along the two angular directions, η and ϕ , and along the calorimeter depth.

The electrodes are longitudinally segmented in three (two) compartments, all called samplings, in the outer (inner) wheel of the calorimeter:

- The first sampling (S1 or front) is about $4.4X_0$ thick in the outer wheel while it is about $22X_0$ in the inner wheel.
- The second sampling (S2 or middle) is about $17X_0$ ($2 - 8X_0$) in the outer (inner) wheel. For particles hitting on the outer wheel most of the energy will be deposited on this second sampling since.
- The third sampling (S3 or back) has a depth between 4 and $12 X_0$, depending on η , in the outer wheel. Note that this compartment is not present in the inner wheel. Sometime it is used to estimate the longitudinal leakage of electromagnetic showers with the data themselves.

Figure 4.6 shows a picture of an electrode corresponding to the outer wheel. The front and back sides correspond to the top and bottom parts of the picture respectively, while pseudorapidity η increases from right to left. The three compartments, S1, S2, S3 can be distinguish by the different segmentation along η they have: the S1 compartment on top of the picture, the S3 on the bottom part and the S_2 in between.

As showed in figure 4.6 the granularity along η is also defined in the electrodes by mean of copper strips using kapton as electrical isolator between them. The size

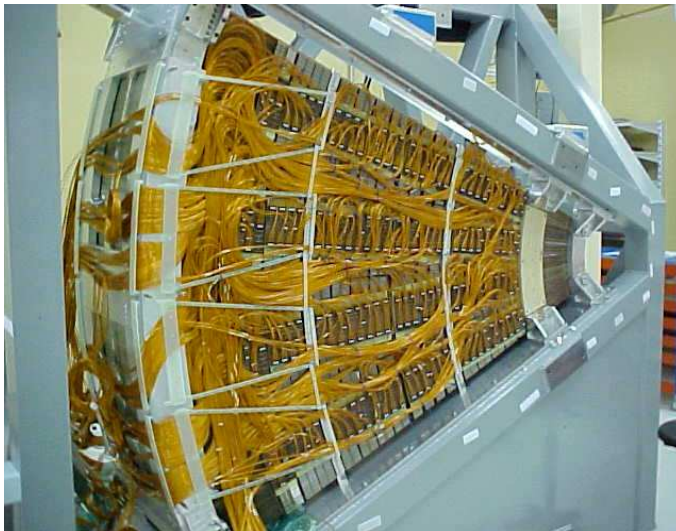


Figure 4.5: Picture of an EMEC module or octant at the stacking frame of the UAM clean room.

of such strips depends on the compartment, being smallest in the S1 to allow for the separation of the two photons from the decay of a π^0 . This separation must be done before the cascade generated by the photons gets broader in the calorimeter material, hence the fine segmentation is defined in the front, S_1 , compartment.³ The values of the cell size for the three compartments as a function of η are given in table 4.1. The strips drawn in the electrodes point to the nominal ATLAS interaction point, however the accordion geometry, for example the absorbers, is not projective to that point.

Wheel	η range	Front	Middle	Back
Outer	1.375 - 1.425	(0.050, $2\pi/64$)	(0.050, $2\pi/256$)	
	1.425 - 1.5	(0.025, $2\pi/64$)	(0.025, $2\pi/256$)	
	1.5 - 1.8	(0.003, $2\pi/64$)	(0.025, $2\pi/256$)	(0.050, $2\pi/256$)
	1.8 - 2.0	(0.004, $2\pi/64$)	(0.025, $2\pi/256$)	(0.050, $2\pi/256$)
	2.0 - 2.4	(0.006, $2\pi/64$)	(0.025, $2\pi/256$)	(0.050, $2\pi/256$)
Inner	2.4 - 2.5	(0.025, $2\pi/64$)	(0.025, $2\pi/256$)	(0.050, $2\pi/256$)
	2.5 - 3.2	(0.1, $2\pi/64$)	(0.1, $2\pi/64$)	

Table 4.1: *Transverse granularity ($\Delta\eta, \Delta\phi$) for each calorimeter sampling (Front, Middle and Back).*

³Regions $|\eta| < 1.5$ and $|\eta| > 2.5$ do not have very fine longitudinal and transversal granularity since they are out of the high precision measurement region. The former corresponds to the barrel-endcap crack (where the large amount of materials in front will not allow to get as good energy resolution as required) and the latter corresponds to very forward regions (with high noise coming from proton remnant and soft interactions).

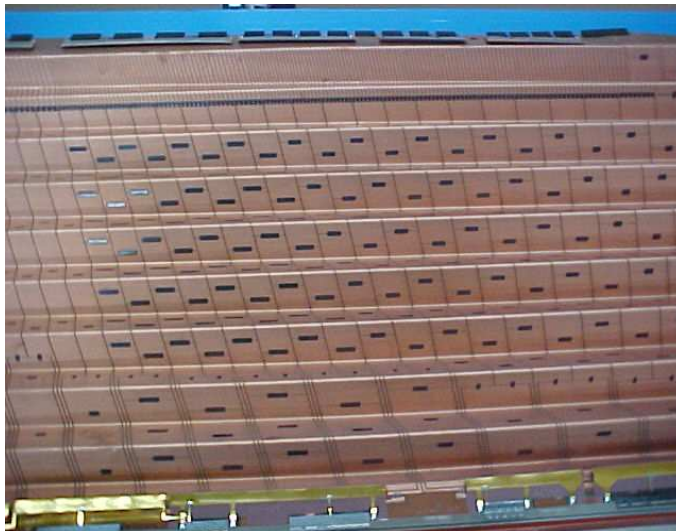


Figure 4.6: Picture of an EMEC electrode of the outer wheel. The segmentation along η and the three compartments in depth, S1,S2 and S3, are clearly seen.

The granularity along the azimuthal ϕ direction is defined by connecting several consecutive electrodes together using the so called summing boards. In principle one could read the electrodes individually, defining a fine granularity along ϕ of 0.003 radians; however this is too much fine for the needs and would increase the number of channels considerably. This is the reason for using Summing Boards (SB) to group the signal of several electrodes together. In this way, for example, in the S2 compartment, three consecutive electrodes are connected (their signals are summed) to obtain the desired granularity of $\Delta\phi = 0.025$ radians, while 12 electrodes are connected for the S1 compartment given a granularity of $\Delta\phi = 0.1$ radians in this compartment. A summary of the EMEC granularity is given in table 4.1.

Figure 4.7 shows some summing boards plugged in the electrode connectors for the S1 compartment of an EMEC module. The ϕ direction goes from bottom to top of the picture, while the η direction increases from left to right. The electrode connectors can be distinguished in black between two absorbers. The summing boards group the signals of 12 electrodes together in this example.

4.4 High Voltage

The relation between the signal (E) and the high voltage (U) applied on the gaps is:

$$E \sim \frac{f_s}{g^{1+b}} U^b \quad (4.1)$$

where g is the liquid argon gap thickness and f_s the sampling fraction (which is a function of the gap thickness). The value for the exponent b was measured at beam beam test of Module 0 to be close to 0.4 [9].

The argon gap of the EMEC decreases almost linearly when the pseudorapidity

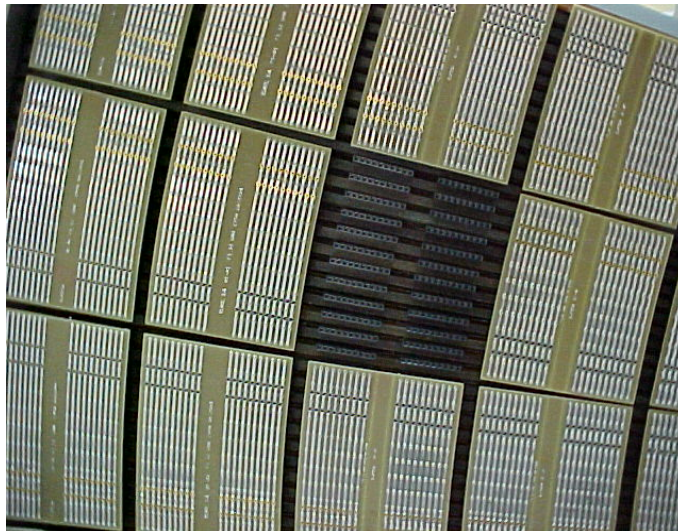


Figure 4.7: Picture the summing boards plugged in the front face of an EMEC module.

	End-cap outer wheel						
HV region	1	2	3	4	5	6	7
η range	1.375-1.5	1.5-1.6	1.6-1.8	1.8-2.0	2.0-2.1	2.1-2.3	2.3-2.5
HV values	2500 V	2300 V	2100 V	1700 V	1500 V	1250 V	1000 V

Table 4.2: *The high voltage regions of the end-cap outer wheel.*

(η) increases. This makes the cluster signal changing along the pseudorapidity direction due to the explicit gap variation and the implicit change in the sampling fraction according to equation 4.1. The sampling fraction (f_s) decreases when η increases, but not fast enough to cancel the $1/g^{1+b}$ rise, as a result the response E increases with η . This growth may be compensated by decreasing U continuously when η increases. For practical reasons a decreasing stepwise function for U is chosen defining seven HV sectors, the High-Voltage sector definitions is given in Table 4.2. for the outer wheel ⁴. Inside one sector the HV is constant and therefore the cluster signal increases with η . To correct for the increase of the cluster signal inside HV sectors, η -dependent weights ($w^{(s)}$) are applied on each cell:

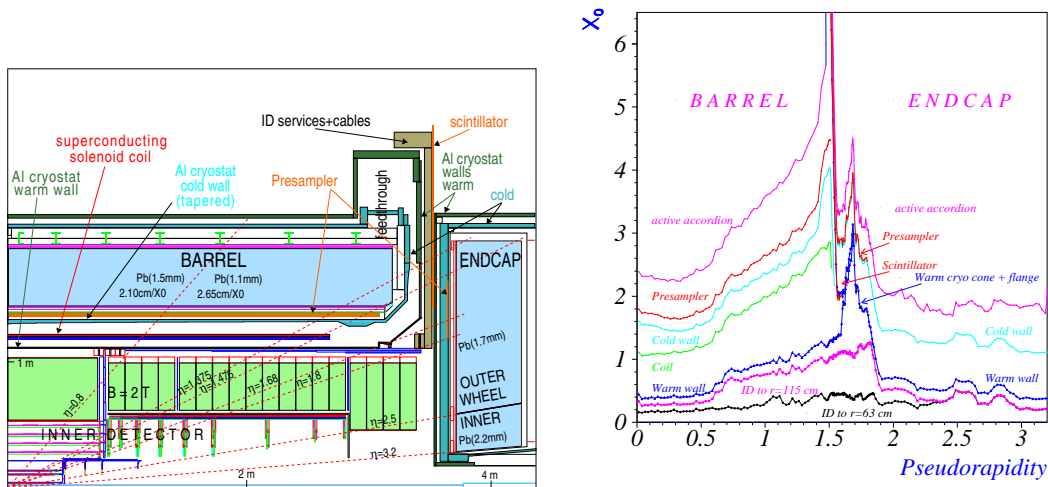
$$w^{(s)}(\eta_j) = \beta^{(s)} / (1 + \alpha^{(s)}(\eta_j - \eta^{(s)})) \quad (4.2)$$

where for a given sampling layer (front, middle or back) η_j is the cell pseudorapidity and $\eta^{(s)}$ the pseudorapidity at the centre of the HV sector s . The parameter $\alpha^{(s)}$ is the slope of the energy dependence with η and the parameter $\beta^{(s)}$ accounts for inaccurate high voltage settings. Both parameters were obtained from a fit to the test beam data [10, 14].

⁴There are two additional sectors in the inner wheel which are not given on the table

4.5 Presampler

In figure 4.8 (a) a schematic view of a quadrant of the electromagnetic calorimeter is shown. An electron, positron or photon created in one p-p collision will cross different layers of material, of the inner detector, cables, boards, cryostat walls, etc, before it enters into the End-Cap Electromagnetic Calorimeter (EMEC). The particle may start a particle-shower (or particle-cascade) crossing these consecutive material layers by the effect of the bremsstrahlung process (photon emission by an electron or positron) or the pair creation process (e^+e^- creation by a photon). Every secondary particle may suffer either the bremsstrahlung process (in case of e^+ or e^-) or pair creation (in case of γ) creating tertiary particles and so on. In this way a cascade is developed. Every charged particle of this cascade will lose part of its energy by ionization of the material. In addition, the $2T$ magnetic field may bent some of the charged particles of the cascade such that they hit the calorimeter at an unexpected position. The result is that the energy measured in the calorimeter will be smaller than the initial particle energy as produced in the p-p collision.



(a) Longitudinal view of a quadrant of the EM (b) Breakdown of the material in front of the calorimeter EM calorimeter

Figure 4.8: Description of the material in front of the calorimeter

The amount of material depends on the η direction, as can be seen in figure 4.8 (b), where the amount of material is expressed in units of radiation lengths (X_0) and it goes up to about $3 - 5X_0$ in the region $1.5 < |\eta| < 1.8$ degrading the measured energy. In order to partially recover this resolution a presampler detector is placed in front of the calorimeter in the region $1.5 < |\eta| < 1.8$. The endcap presampler is divided into 768 cells per endcap wheel with a transversal segmentation of $\Delta\eta \times \Delta\phi = 0.025 \times 2 \cdot \pi/64$. The quoted segmentation along ϕ is achieved by the modularity in 32 identical azimuthal modules. Each module consist of two active Liquid Argon layers, 2 mm thick, formed by three electrodes parallels to the front face of the EMEC.

Figure 4.9 shows the material in front of the calorimeter for the η region studied

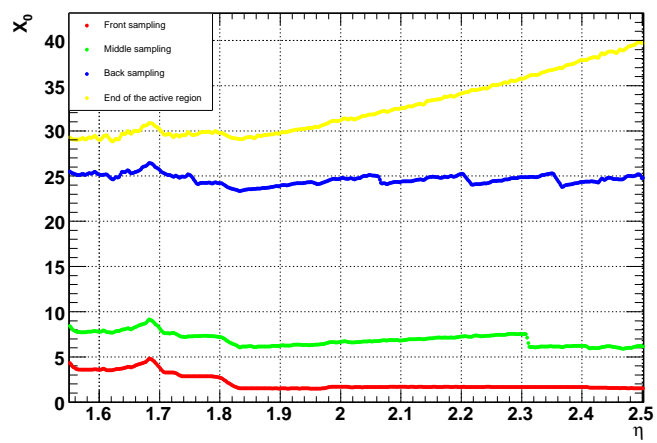


Figure 4.9: *Total amount of material in front of the different samplings of the EMEC in the η region of interest.*

in this document.

Chapter 5

The Calibration Hits method

An electron (or a photon) deposits energy in several cells of the calorimeter due to EM shower created by the interaction with matter. A cluster of cells is then defined to contain the energy deposits, or at least most of them, in order to compute the electron (photon) energy. However, several effects distort this calculation, namely: the energy lost by the electron (photon) in the matter in front of the calorimeter, the energy leaked behind the calorimeter and the energy outside the defined cluster of calorimeter cells. A method to correct for these energy losses and reconstruct the electron (and photon) energies from the cluster energies deposited in the active layers of the calorimeter and the presampler has been applied to the Barrel Electromagnetic Calorimeter (EMB) [12]. The method is built in a modular way and the corrections are parametrized as a function of measurable quantities: energies in presampler, front, middle and back calorimeter layers and the barycenter in depth. The parameters are obtained from a special Monte Carlo simulation, labeled Calibration Hits, which includes the energy deposits in all materials of the detector and not only in the active ones. In this document the method is applied to the EM EndCap Calorimeter (EMEC), taken into account the peculiarities of this device: different geometry, different dead material in front and the presampler does not cover the whole range in pseudorapidity (η). These differences between the EMEC and the EMB forced us to do some modifications in the Calibration Hits method, in particular in the region without presampler a new algorithm has to be developed to recover the energy lost in front of the EMEC. For this work, electrons are simulated from the nominal Atlas interaction point taken into account the magnetic field (which deflects electrons) and the interaction vertex spread (due essentially to the z -width of the LHC proton bunches).

5.1 Cluster Energy

When an electron or photon goes through the ATLAS Calorimeter it deposits part of its energy in several cells of the different layers. In order to reconstruct the energy of the incoming particle a cluster of cells in (η, ϕ) is defined around the cell with maximum deposit. The cluster size should not contain many cells to avoid introducing too much

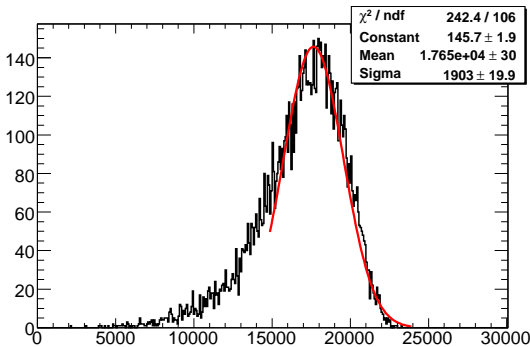


Figure 5.1: Cluster energy distribution for 100 GeV Monte Carlo electrons at $\eta = 1.7125$. Calibration Hits Method is not applied to the events. A gaussian fit is superimposed.

noise in the signal, however it should contain enough energy of the electron or photon cascade. There are two sources of noise: the readout electronics and the minimum bias events, physics low energetic events which superimpose the hard process under study. The choice of the cluster size is then a compromise between minimizing the noise in the cluster and minimizing the cascade energy leaked out of the cluster. A small amount of cascade energy leaking out of the cluster can be recovered using the Calibration Hit method as illustrated in a subsequent section.

In the present work, three different choices of cluster size are studied: 3×5 , 3×7 and 5×5 . The first number refers to the number of cells of the middle compartment of the calorimeter along the η direction, while the second number is the number of cells of the middle compartment of the calorimeter along the ϕ direction. The corresponding cells of the other two compartments, Front and Back, complete the cluster definition.

The sum of the energies deposited in each cell of the cluster will be named "cluster energy". As an example, a 3×7 cluster energy distribution for 100 GeV electrons is represented in figure 5.1 before the Energy Reconstruction method (the Calibration Hit method) is applied to perform the corrections mentioned above. A gaussian fit is plotted as well to observed the deviation of the distribution from a gaussian shape.

The clustering algorithms allow also to determine the pseudorapidity of the incoming particle using only information from the calorimeter. This variable is computed as the following barycenter along η :

$$\eta_{calo} = \frac{\sum_s \eta_c^s \cdot E_s}{\sum_s E_s}$$

where η_c^s and E_s are the central η value and the energy deposit on the s th cell and s runs over all the cells forming the cluster. In this document we will refer to this magnitude as η since we are only using calorimeter information.

5.2 Description of the method

When an electromagnetic cluster in the EM Calorimeter is identified, the energy contained in this cluster of calorimeter cells is less than the energy of the electron (or photon). This is due to energy losses in the dead material in front of the calorimeter and the leakage both lateral outside the cluster and longitudinal behind the calorimeter. To recover the electron (photon) "true" energy from the measured cluster energy, corrections for the three energy losses are applied. These corrections are functions of measured quantities such as the energies on the three layers of the calorimeter, E_1, E_2, E_3 , the energy on the presampler, E_{ps} and η of the incoming particle. The corrected cluster energy will be called E_{reco} and it is split in three terms, namely:

$$E_{reco} = E_{infront} + E_{calo} + E_{behind} \quad (5.1)$$

where $E_{infront}$ corresponds to the cluster energy corrected for the effect of the material in front of the calorimeter, E_{calo} is the cluster corrected for two effects occurring inside the calorimeter, the lateral leakage outside the cluster and a small bias in the sampling fraction, and E_{behind} refers to the cluster energy corrected for the longitudinal leakage behind the calorimeter. These corrected energies are functions of $E_{ps}, E_1, E_2, E_3, \eta$, and the longitudinal barycenter X , defined as the following linear combination:

$$X = \frac{\sum_{i=1}^3 X_i \cdot E_i}{\sum_{i=1}^3 E_i} \quad (5.2)$$

$X_i, i = 1, \dots, 3$ being the compartment, S1, S2, S3, geometrical centers in units of radiation length (X_0).

These functions are written along this document as:

-

$$E_{calo} = f_{calo}(\eta, X) \cdot (1 + f_{out}(\eta, X)) \cdot \sum_{i=1}^3 E_i$$

where f_{out} is the correction to recover the lateral leakage out of the cluster and f_{calo} is a small correction to the sampling fraction taking into account in E_1, E_2, E_3 .

-

$$E_{behind} = E_{calo} \cdot f_{leak}(\eta, X)$$

where f_{leak} refers to the correction for leakage behind the calorimeter

- For region with presampler:

$$E_{infront} = a(\eta, E_{calo}) + b(\eta, E_{calo})E_{ps} + c(E_{calo}, \eta) \cdot E_{ps}^2$$

For region without presampler:

$$E_{infront} = a(\eta, E_{calo}) + b(\eta, E_{calo})X + c(\eta, E_{calo})X^2$$

To determine the weights (or coefficients) entering the above formula for the reconstructed energy, a Monte Carlo simulation of the ATLAS nominal setup is performed using ATHENA 12.0.3 (the official ATLAS software) which incorporate the Monte Carlo program GEANT 4.7 for the simulation of the particle-matter interactions. This simulation includes the energy deposits in both passive and active parts of the detector. Digitization and reconstruction ¹ stages are included to profit from extra information as the presence of tracks, to distinguish between electrons and photons, or EM particle identification (*IsEm*), to determine the quality of electrons. After these stages, cell energies are corrected by the effect of the gap size variation with η inside high voltage regions of the EMEC (see equation 4.2).

In order to extract a full set of coefficients for every correction in the pseudorapidity region corresponding to the endcap a set of 220000 electrons per energy have been generated, for the following energies: 25, 50, 75, 100, 200 and 500 GeV. The CPU time needed per event simulated depends on the electron energy and it goes from 7 minutes at 25GeV, up to 15 minutes at 500GeV. All of the events have been produced using the Grid computing site of our Laboratory at UAM. To increase statistical significance, all the fits of this work, were done taking into account only histogram bins in which the number of events were higher than 0.5 percent of the total.

5.3 Corrections for energy depositions in the calorimeter

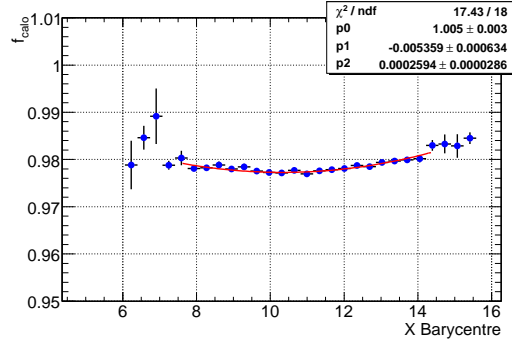
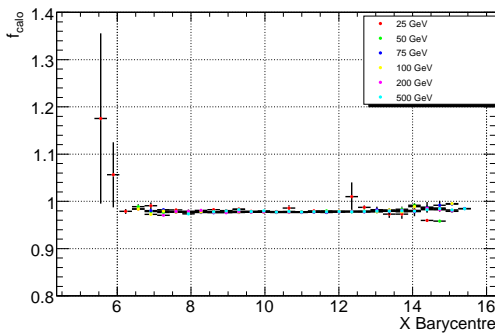
The digitization+reconstruction step performed over the single electrons samples used on this analysis allow to apply a correction factor taking into account the High Voltage and sampling fraction variation with η , providing an approximation for energies, E_1, E_2, E_3 , deposited in the front, middle and back compartments respectively. The correction factor f_{calo} is then defined as the ratio between the total energy in

¹The simulation of ATLAS events is performed in five steps: Generation (where the cinematics of the event is produced), Simulation (where GEANT emulates the interaction of every particle with matter), Digitization (where the readout and all the electronics is simulated), Reconstruction (where all variables of interest are computed from raw data) and ESD and AOD production (those last steps produce standard object to work with when doing physics analysis). Even though we are working at the simulation level, we run the two following steps to get the information needed for particle identification.

the calorimeter given by the Monte Carlo over the total energy obtained after the digitization+reconstruction step mentioned above, namely:

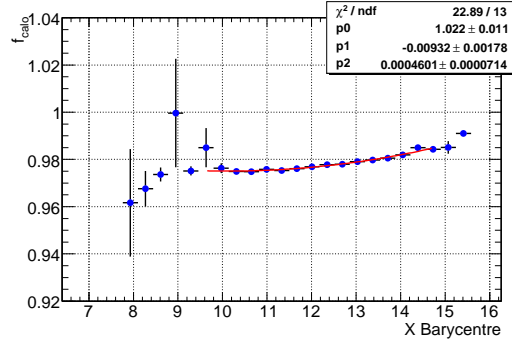
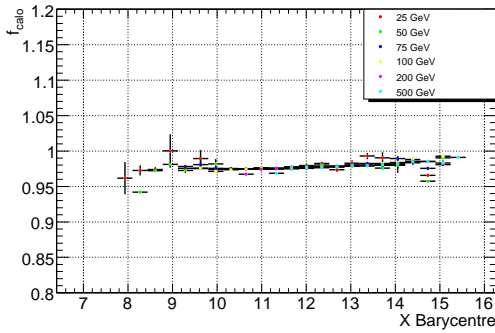
$$f_{calo}(\eta, X) = \frac{\sum_{i=1}^3 E_i^{abs} + E_i^{lar}}{\sum_{i=1}^3 E_i}$$

where E_i^{abs} (E_i^{lar}) is the energy deposited on the absorbers (LAR) of the i th compartment of the calorimeter. In figure 5.2 (left) this factor is represented versus X for two values of η , 1.7125 and 1.9125, for all the energies. It can be observed a small deviation, of about 2 %, respect to unity reflecting an overestimation of the energy in the digitization+reconstruction step.



(a) f_{calo} versus X for the various energies at $\eta = 1.7125$

(b) f_{calo} versus X (energy averaged) at $\eta = 1.7125$



(c) f_{calo} versus X for the various energies at $\eta = 1.9125$

(d) f_{calo} versus X (energy averaged) at $\eta = 1.9125$

Figure 5.2: f_{calo} correction as a function of the longitudinal barycenter of the shower

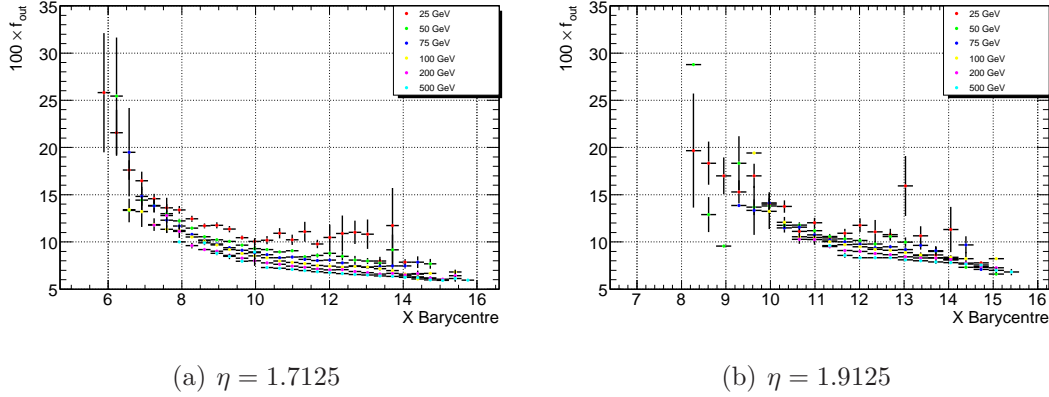
The distributions shown in figure 5.2 correspond to a profile of the factor f_{calo} versus X , i.e, we fixed a certain number of X bins and for each of those bins we build a f_{calo} distribution. The final plots show the mean value of the distribution versus the center of the X bin.

The correction is parametrized as a function of the barycenter of the shower X . The slight deviation from one shows that the estimated sampling fraction and H.V correction applied at the construction step is overestimated.

The correction is rather independent of energy, hence an average over all energy points is obtained and fitted to a second order polynomial (figures 5.2 b and d) with coefficients being η dependent²:

$$f_{calo}(\eta, X) = q_0(\eta) + q_1(\eta) \cdot X + q_2(\eta) \cdot X^2 \quad (5.3)$$

²The η dependence means that a set of parameters has been determined for each η -middle-cell value

Figure 5.3: f_{out} correction as a function of X for the different particle energies

5.4 Correction for lateral leakage out of the cluster

The second factor which contributes to the term E_{calo} in (5.1) is (f_{out}) which is determined by the energy leaked out transversally of the cluster. It is defined by (5.4):

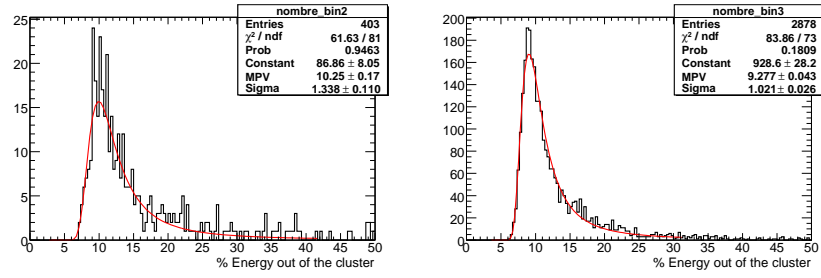
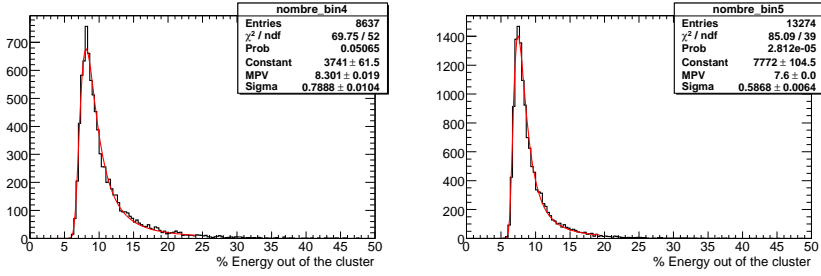
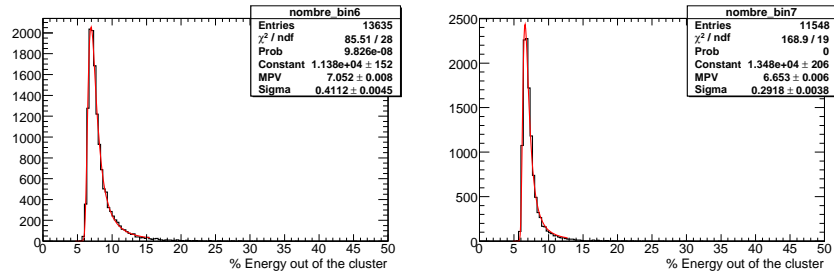
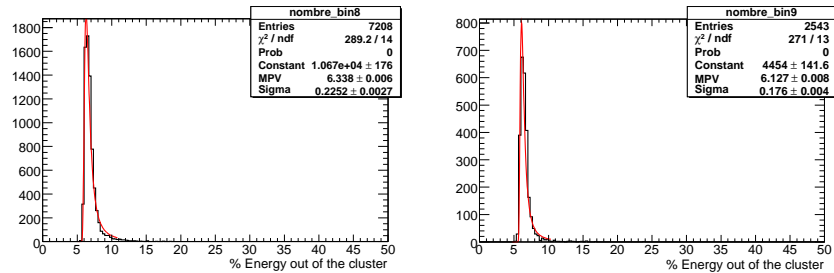
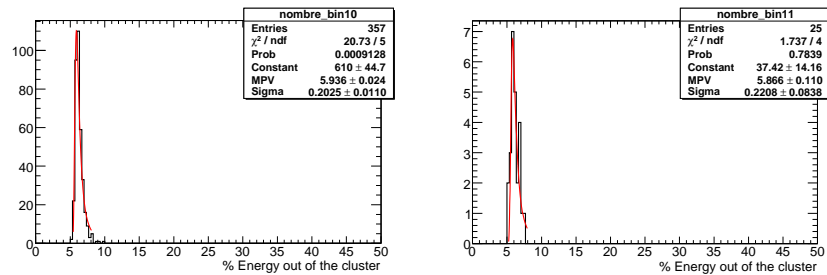
$$f_{out}(\eta, X) = \frac{\sum_{i=1}^3 E_{cl,i}^{out}}{\sum_{i=1}^3 (E_{cl,i}^{abs} + E_{cl,i}^{act})} \quad (5.4)$$

where $E_{cl,i}^{out}$ is the energy out of the cluster in the i th layer and i runs to the three layers (Front, Middle and Back). In contrast to the f_{calo} correction, f_{out} shows an energy dependence (see figure (5.3)) due to the fact that the low energy electrons are more deflected by the magnetic field. However, the energy independence of this corrections is recovered by treating the distributions of f_{out} belonging to a determined X bin in a special way. As it is shown in figure (5.4), the distributions have really long tails in the low X bins while they are gaussian-like distributions when we look at higher X bins. The adopted approach is to fit all distributions with a landau-like function and use the Most Probable Value (MPV) + one standard deviation (σ) as a function of X (where X refers to the center of the bins specified). It can be observed in figure 5.5 (a) that using MPV+ σ the correction is rather independent of energy. This procedure also prevents for underestimation of the reconstructed energy specially at low values of the generated electron energy.

An average over all energies is represented in figure 5.5. The points are fitted by the following function:

$$f_{out}(\eta, X) = p_0(\eta) + p_1(\eta) \cdot X + \frac{p_2(\eta)}{X} \quad (5.5)$$

In this procedure it was assumed that the particle is incident at the center of the central cell of the cluster. This is obviously not always the case and must be taken

(a) $6 < X < 7$ (b) $7 < X < 8$ (c) $8 < X < 9$ (d) $9 < X < 10$ (e) $10 < X < 11$ (f) $11 < X < 12$ (g) $12 < X < 13$ (h) $13 < X < 14$ (i) $14 < X < 15$ (j) $15 < X < 16$ Figure 5.4: f_{out} distributions per X bin at $\eta = 1.7$

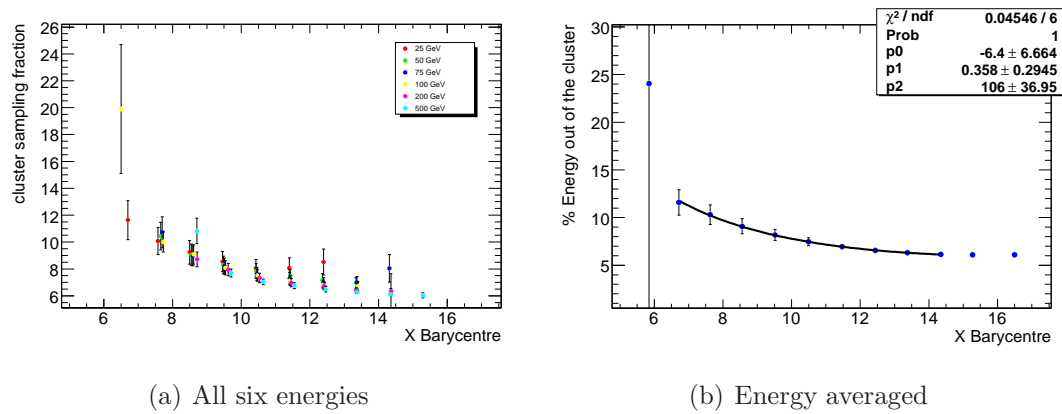


Figure 5.5: $MPV + \sigma$ of the f_{out} distributions as a function of the Barycentre of the shower X

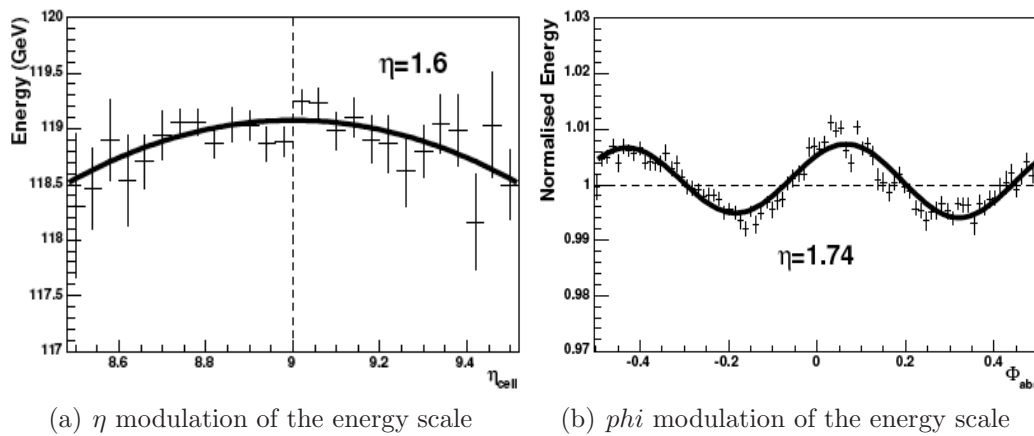


Figure 5.6: η and ϕ modulations observed on the beam test.

into account in a second step of the Calorimeter Reconstruction Algorithm. In order to be more clear, figure 5.6 shows the observed η (left plot) and ϕ modulation during beam tests. The η modulation shows clearly the increase of energy underestimation when the incident electron hits farther away from the center of the cluster. In the ϕ modulation plot a combination of leakage and irregularity effect due to the accordion geometry is shown. Notice that these corrections are applied in a step after the calibration hits method using the information extracted from the test beam. Therefore, all results presented in subsequent sections still need to be corrected by those modulations.

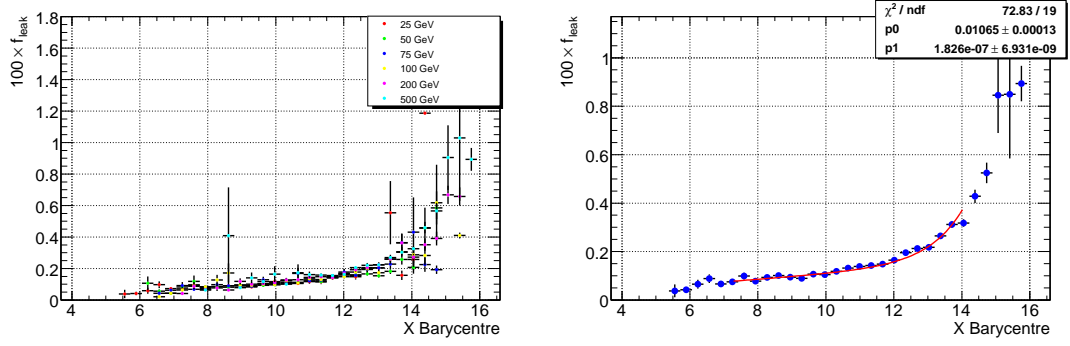
5.5 Corrections for longitudinal leakage

The small fraction of the energy that is deposited behind the calorimeter is computed by applying to the reconstructed energy in the calorimeter the factor f_{leak} , defined

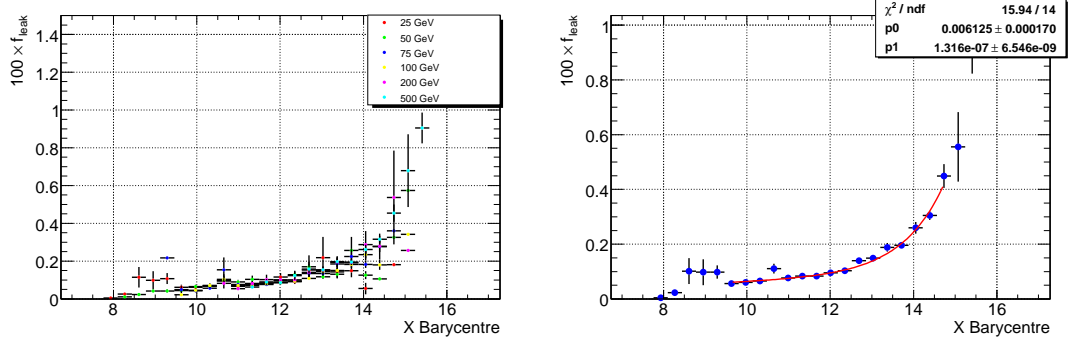
by (5.6):

$$f_{leak}(\eta, X) = \frac{E_{leak}}{E_{acc}} \quad (5.6)$$

where E_{leak} accounts for all the energy deposited behind the calorimeter and E_{acc} for all the energy depositions in the calorimeter (active and pasive materials). As shown in figure (5.7 a and c), f_{leak} is again fairly energy independent when it is parameterized as a function of the longitudinal barycenter of the shower.



(a) f_{leak} versus X for the various energies at $\eta = 1.7125$ (b) f_{leak} versus X (energy averaged) at $\eta = 1.7125$



(c) f_{leak} versus X for the various energies at $\eta = 1.9125$ (d) f_{leak} versus X (energy averaged) at $\eta = 1.9125$

Figure 5.7: f_{leak} correction as a function of the longitudinal barycenter of the shower

The weights that corrects for the longitudinal leakage are extracted by fitting the energy averaged f_{leak} distributions to the following function (figure 5.7 b and d):

$$f_{leak}(\eta, X) = l_0(\eta) \cdot + l_1(\eta) \cdot e^X \quad (5.7)$$

The η dependence of these parameters reflects the variation of the calorimeter depth with η .

5.6 Corrections for the energy loss in front of the Calorimeter

In [12] is demonstrated that the energy lost in front of the calorimeter (inner detector, cryostat, boards, cables, material between presampler and S1) can be successfully parameterized as a function of the energy deposited in the presampler detector of the EM Barrel Calorimeter. However, in the EMEC only the region $\eta < 1.8$ is equipped with a presampler. For the region $\eta > 1.8$ a new procedure has been developed in the present work.

5.6.1 Region with presampler $\eta < 1.8$

As in the case of f_{out} a special treatment of the distributions of energy in front of the calorimeter per presample energy (E_{ps}) bin was done. In figure 5.8 we can see that the distributions of energy in front of the calorimeter are landau-like at low energy depositions in the presampler while they are more gaussian-like when the energy deposit is higher. The treatment consist on taking the most probable value of the distributions (instead of the mean value) by using a gaussian fit in the interval $(1.0 \cdot \sigma, 1.5 \cdot \sigma)$ around the maximum. The fit is also represented in the figure. Figure 5.9 shows the difference between considering the most probable value of the distributions and considering the mean for $25 GeV$ electrons being incident at $\eta = 1.7$. The proper choice in this approach has an impact on the energy resolution and energy scale.

The energy in the dead material in front of the calorimeter, obtained as the most probable value fit described above, is represented versus the energy deposited in the presampler at $\eta = 1.6125$ in figure 5.10. The six different plots correspond to the six different electron energies.

The points are fitted using the following second order polynomial:

$$E_{infront} = a(E_{calo}, \eta) + b(E_{calo}, \eta) \cdot E_{ps} + c(E_{calo}, \eta) \cdot E_{ps}^2 \quad (5.8)$$

The fit includes a quadratic term, which is absent for the EMBarrel, due to the larger variation of material in front for the EMEC. We notice a dependence with energy which is considered by making the coefficients of the polynomial dependent on E_{calo} .

Similar plots are represented in figure 5.11 for a different value of pseudorapidity, $\eta = 1.7125$. There are small variations with respect to $\eta = 1.6125$, which results on different paramaters for the fit using the polynomial 5.8.

Figure 5.12 represents the parameters of the previous fit as a function of E_{calo} . The left column of plots refers to $\eta = 1.6125$ and the second one to $\eta = 1.7125$. The points are fitted to the following functions:

$$a(E_{calo}, \eta) = O_0(\eta) + O_1(\eta) \cdot E_{calo} + O_2(\eta) \cdot \sqrt{E_{calo}} \quad (5.9)$$

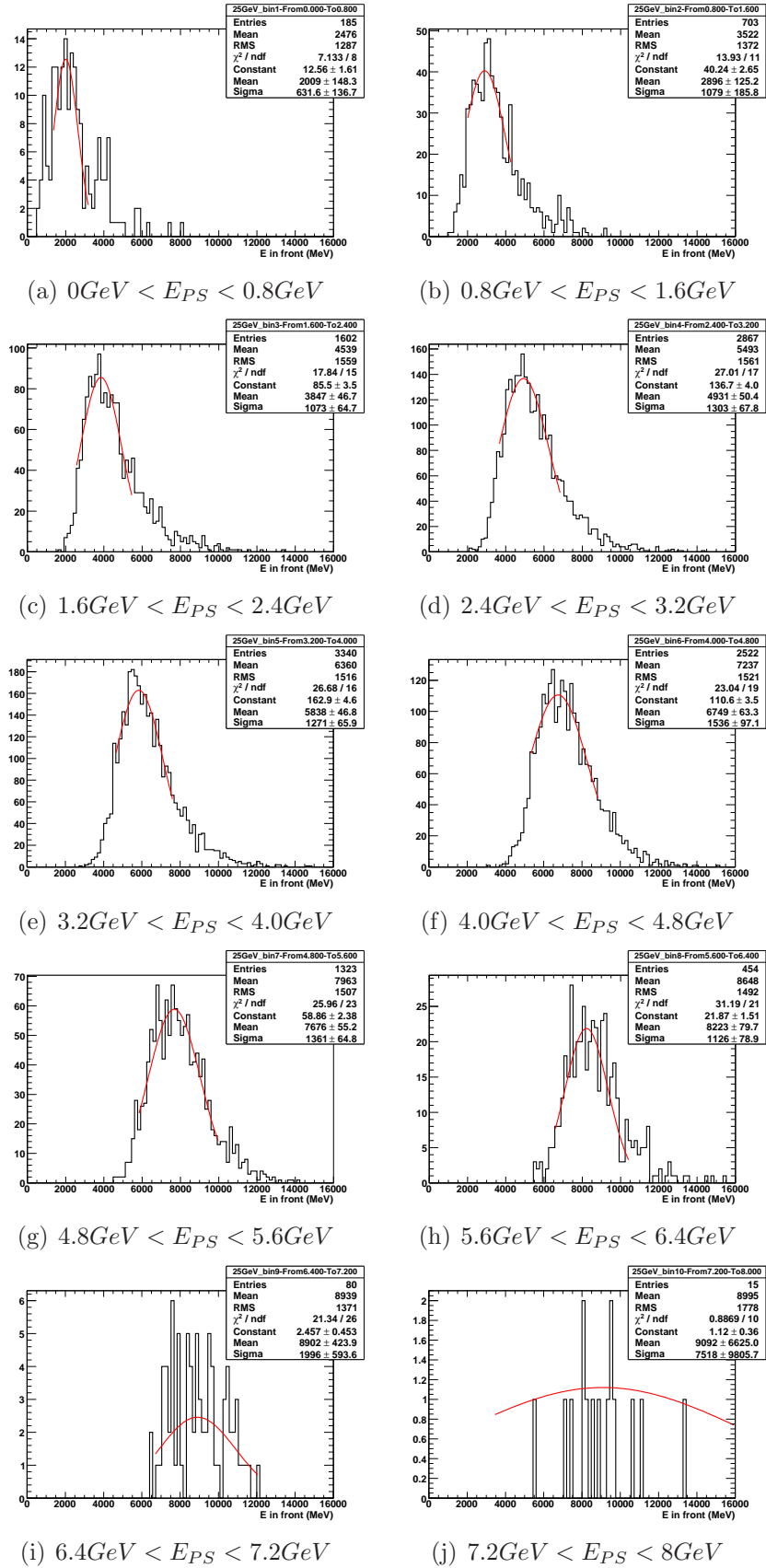


Figure 5.8: Distributions of energy in front of the calorimeter per E_{PS} bin at $\eta = 1.7$ for 25GeV electrons

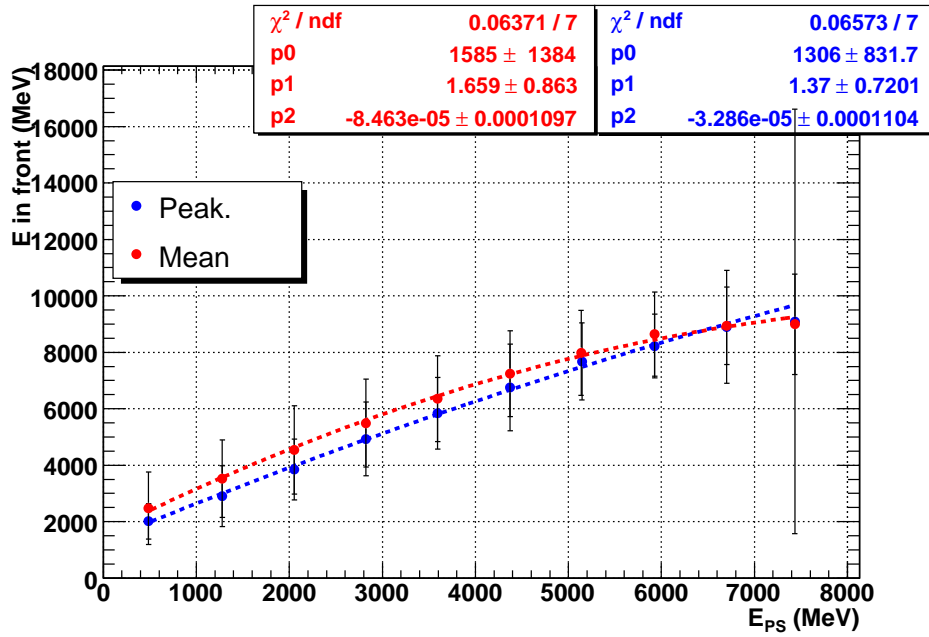


Figure 5.9: Energy in front of the calorimeter versus E_{PS} for the two different approaches. The blue points represent the mean of the E in front distributions for E_{PS} while red points represent the peak of the distributions..

$$b(E_{calo}, \eta) = S_1(\eta) + S_2(\eta) \cdot \text{Log}(E_{calo}) + S_2(\eta) \cdot \sqrt{E_{calo}} \quad (5.10)$$

$$c(E_{calo}, \eta) = R_1(\eta) + R_2(\eta) \cdot E_{calo} - \frac{R_3(\eta)}{E_{calo}^2} \quad (5.11)$$

The fact that the offset a is not negligible means that there can be energy lost in the material in front and however no energy deposited in the presampler. This effect has two sources:

i) the material between the presampler and the S1-compartment of the calorimeter, electronics and cables, is considered as material in front of the calorimeter, but it is behind the presampler;

ii) absorption of very low energy photons and electrons present in the early shower.

According to equation 5.9 this offset increases with E_{calo} .

Parameter b is a kind of "gain" factor to convert from E_{ps} signal to $E_{in,front}$. Parameter c takes into account small non-linearities or saturation effects.

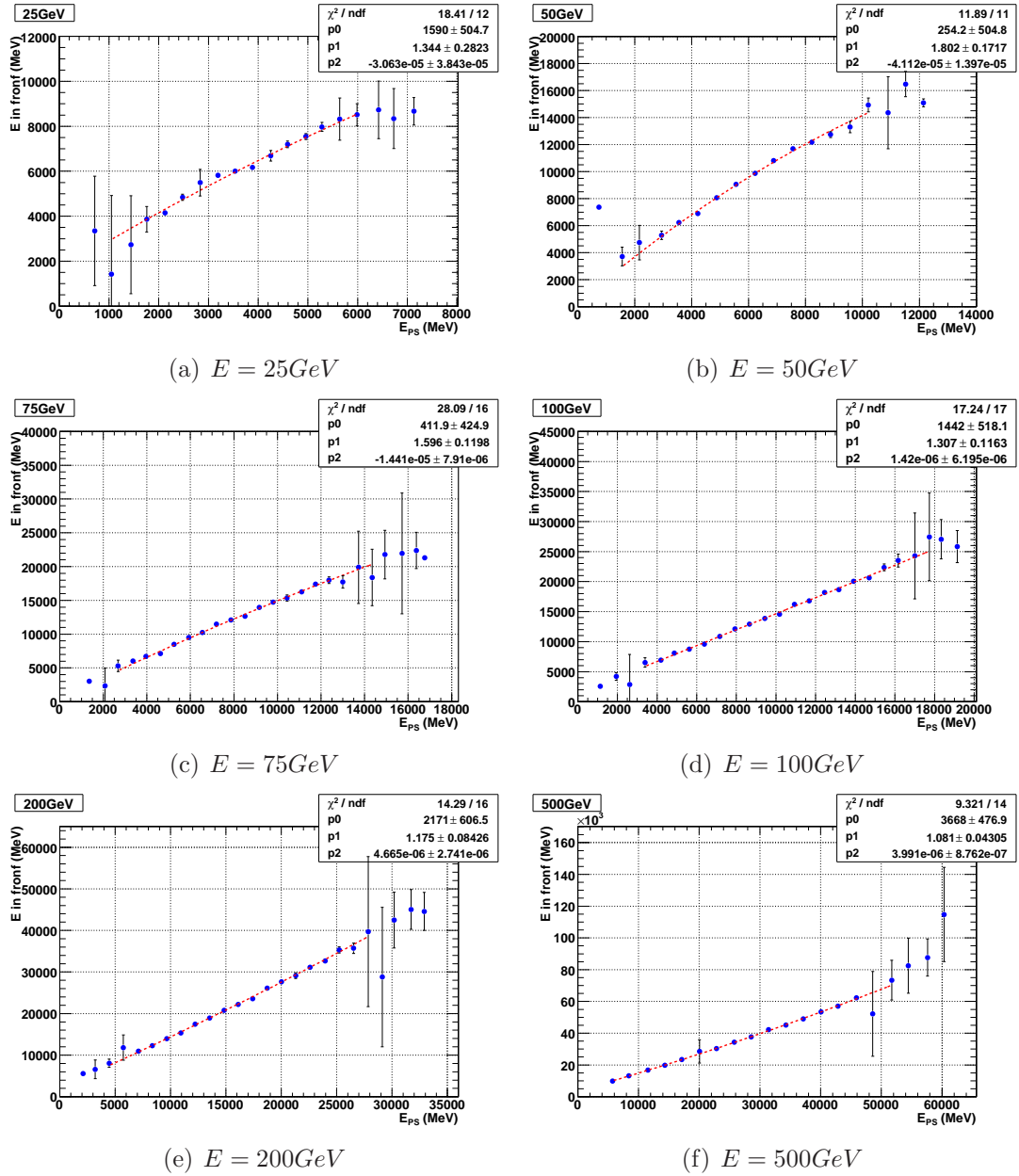


Figure 5.10: Energy in front of the calorimeter versus energy in the presampler for different electron energies at $\eta = 1.6$

5.7 Region without presampler $\eta > 1.8$

As explained before, the Calibration Hits method in the $\eta < 1.8$ region is basically an adaptation of the already existing method for the EMBarrel. However, for $\eta > 1.8$ a new approach has been developed trying to use variables sensitive to the upstream material, since no presampler is present in this region. Two different procedures have been tried and compared: a parameterization of the energy lost as a function of X , and the use of the S1 compartment as a kind of presampler.

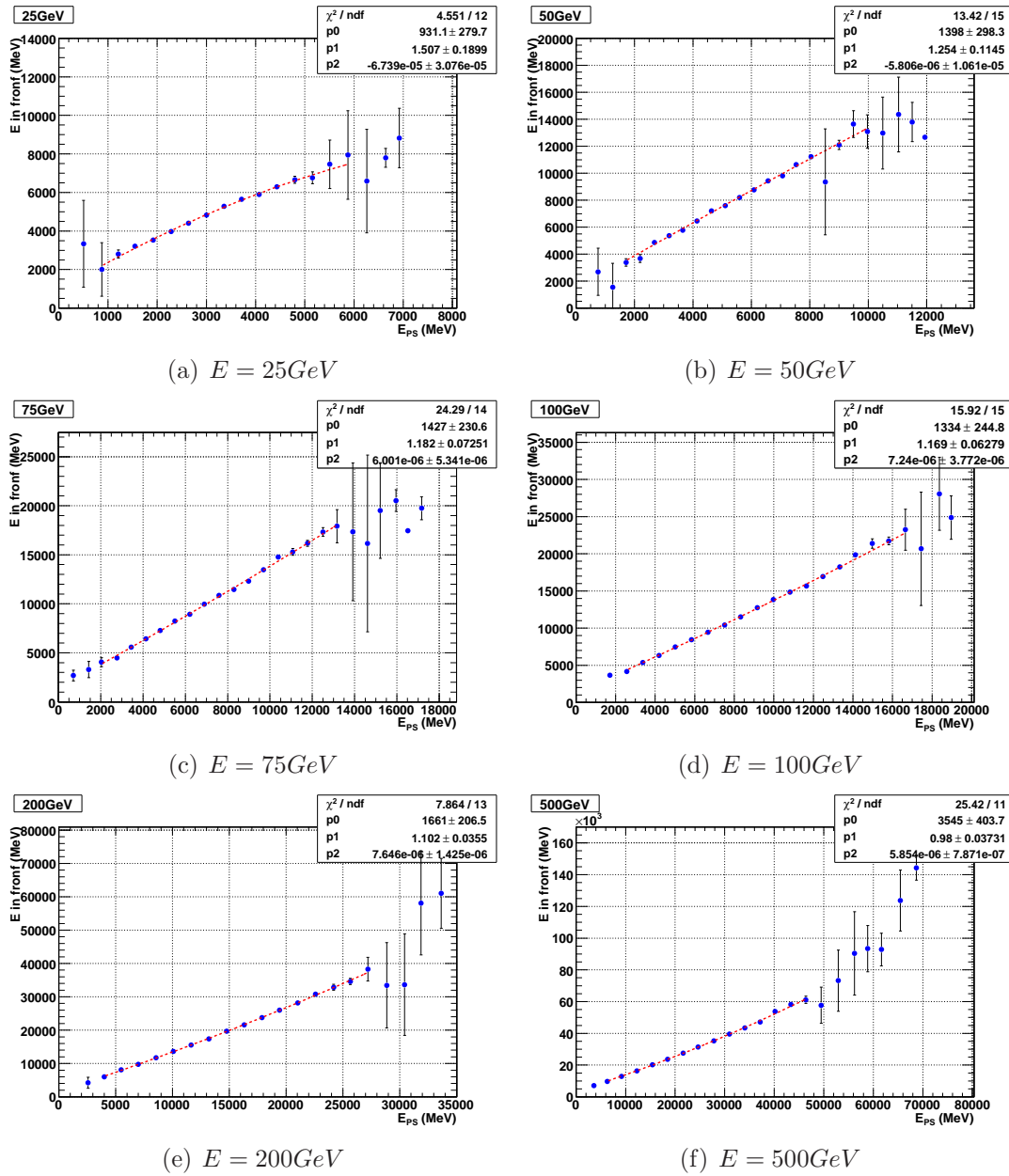


Figure 5.11: Energy in front of the calorimeter versus energy in the presampler for different electron energies at $\eta = 1.7$

1. Parametrization of the energy lost in front of the calorimeter as a function of X . The barycenter in depth X is expected to change by the presence of upstream material due to the early start of the shower. More energy lost in the upstream material would mean less value for X and vice versa, less energy lost in front of the calorimeter would mean larger value for X . Figure 5.14 represents the energy lost in front as a function of the barycenter of the shower X . The points are obtained as the most probable value of the distributions following a similar procedure as described in previous section. From figure 5.14

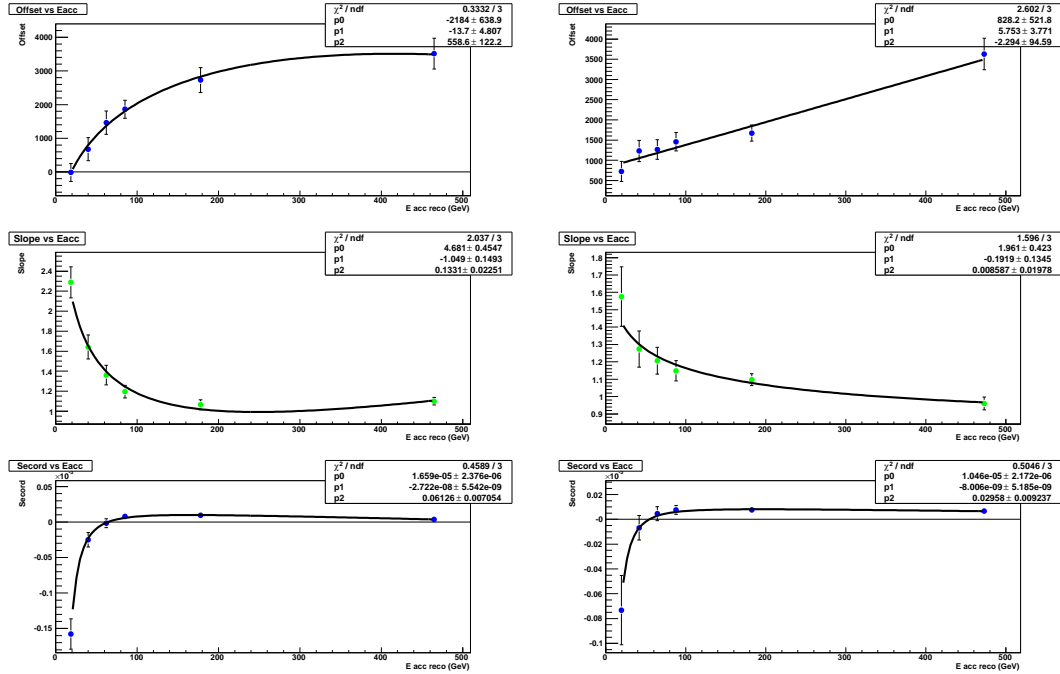
(a) $\eta = 1.6$ (b) $\eta = 1.7$

Figure 5.12: Parameters a, b, c of equation 5.8 as a function of E_{calo} . The left side column corresponds to $\eta = 1.6$, while the right side column corresponds to $\eta = 1.7$.

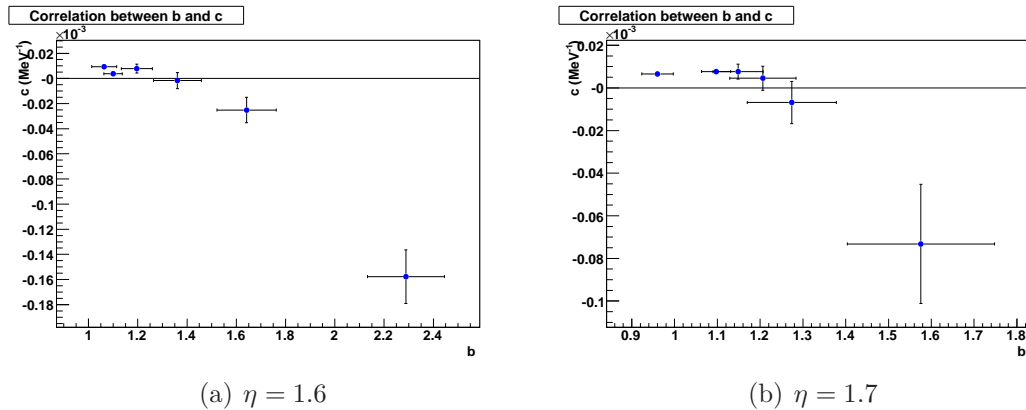
(a) $\eta = 1.6$ (b) $\eta = 1.7$

Figure 5.13: Parameter c versus parameter b of equation 5.8

it can be inferred the sensitivity of the variable X to the energy loss in front of the calorimeter: the more energy loss the smaller the value of X . This relation can be described by a second order polynomial, namely:

$$E_{infront} = a(E_{calo}, \eta) + b(E_{calo}, \eta) \cdot X + c(E_{calo}, \eta) \cdot X^2 \quad (5.12)$$

The dependences of the a, b, c parameters with E_{calo} are shown in figure 5.15. In contrast to the equivalent parameters in the region with presampler, discussed in previous section, this energy dependences is more simple and can be parametrized using second order polynomials.

2. Method of Using the S1 compartment as a presampler. An increase of material in front of the calorimeter would increase the probability of having an early electromagnetic shower with a higher number of particles in its first stages. A larger number of particles entering the S1 compartment would deposit more energy in it, hence the energy in S1 may be sensitive to the amount of energy lost in the upstream material. In general, the thinner a detector layer is, the more sensitive will be to the energy lost in front of it³. The sensitivity is related to the ratio between the energy lost in dead material and the energy deposited in the layer. In the case of the S1 compartment the thickness is about $4.4 X_0$, hence it is expected some sensitivity.

The energy lost in front of the calorimeter as a function of the energy in the S1 compartment (E_1) is shown in figure 5.16. Similarly to the previous sections, the points are produced using the most probable value of the distributions, according to the procedure described in section 5.6.1. It can be observed that the sensitivity of E_1 to the energy loss in front is similar to the sensitivity of X , discussed in previous section, except for the low energy point $E = 25 \text{ GeV}$ (lower slope in the plot). We saw a much larger sensitivity at $E = 25$ using the presampler for $\eta < 1.8$, as shown in figure 5.11. This means that at low energies like 25 GeV the approximation of using the S1 compartment as a presampler is not valid anymore. The reason is related to the position of the maximum of the electromagnetic cascade in the calorimeter. At low input energy this maximum is located closer to the S1 layer, hence too much energy of the cascade is deposited in this compartment to be considered as a "thin" presampler layer. For high input energies less energy, relative to the total, is deposited in S1, hence more sensitivity to the small energy lost in the upstream material.

The energy lost in front of the calorimeter is parametrized by a second order polynomial of the energy deposited in layer S_1 (E_1), as follows:

$$E_{infront} = a(E_{calo}, \eta) + b(E_{calo}, \eta) \cdot E_1 + c(E_{calo}) \cdot E_1^2 \quad (5.13)$$

³Consider that the thickness must be above a certain threshold to get a clean signal out of the detector

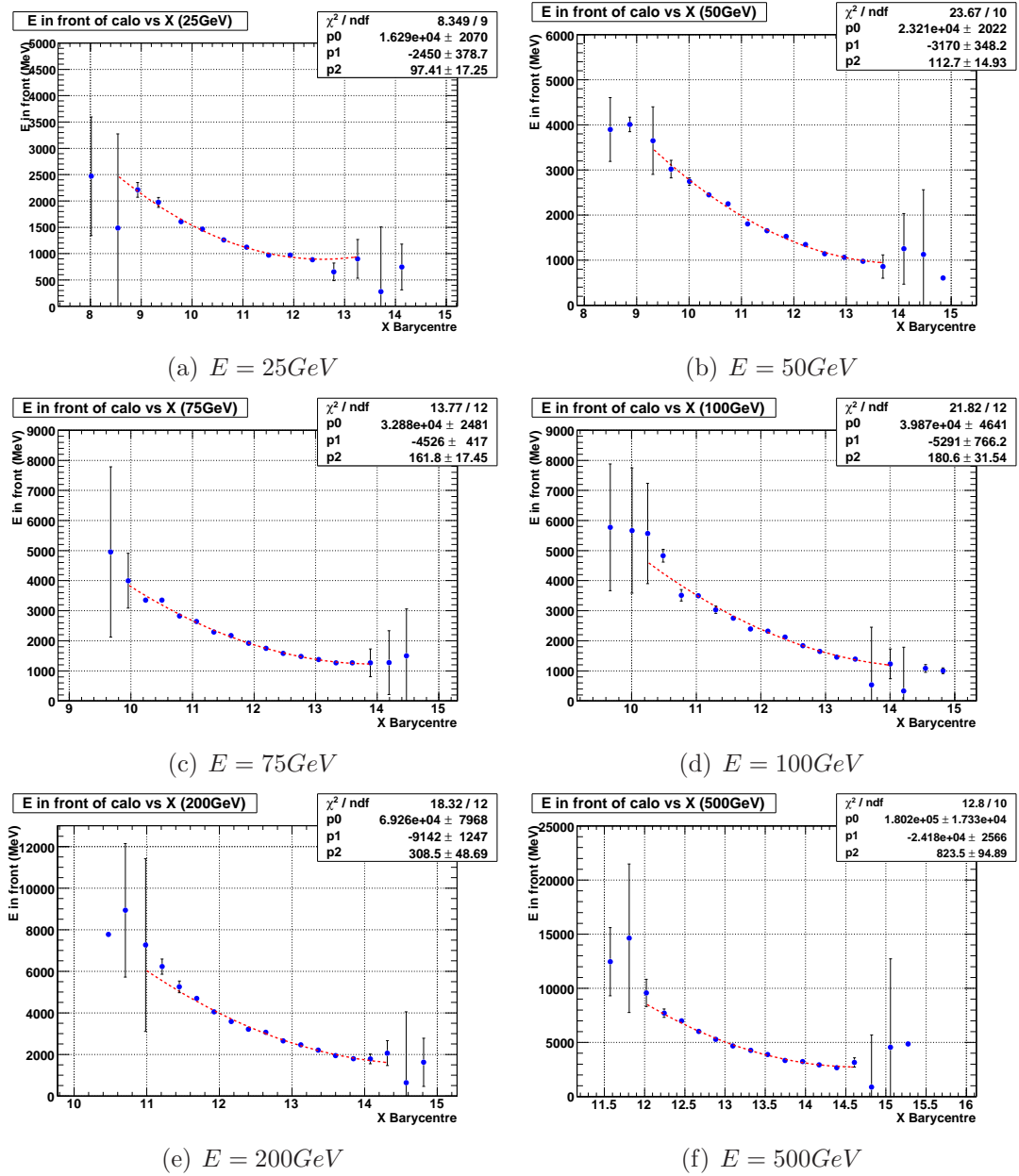


Figure 5.14: Energy in front of the calorimeter versus barycenter of the shower for different electron energies at $\eta = 1.9$

The good quality of the fits can be seen in figure 5.16.

The dependences of the a, b, c parameters with E_{calo} are represented in figure 5.15, and can be fitted using the following functions:

Figure (5.17) shows the energy dependence of all three parameters in the previous fits. Again we observe that all points but the ones corresponding to low energy (25 GeV) follow a certain tendency. The adopted criterium is to eliminate this low energy point from the fit in order to get the coefficients. The extrapolation of the fit to low energies produces good results, as it will be

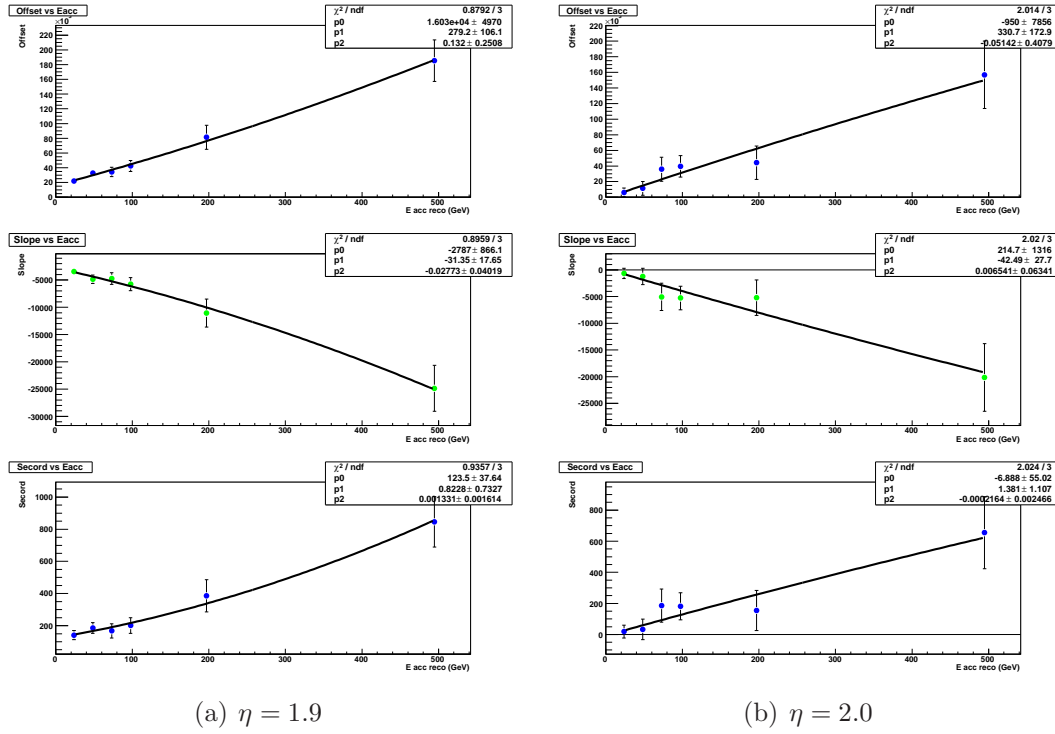


Figure 5.15: Parameters a, b, c of equation 5.12 as a function of E_{calo} . The left side column corresponds to $\eta = 1.9$, while the right side column corresponds to $\eta = 2.0$.

shown in next sections. The functions used to fit the parameters are:

$$a(E_{calo}, \eta) = O_0(\eta) + O_1(\eta) \cdot E_{calo} + O_2(\eta) \cdot \sqrt{E_{calo}} \quad (5.14)$$

$$b(E_{calo}, \eta) = S_1(\eta) + S_2(\eta) \cdot \text{Log}(E_{calo}) + S_2(\eta) \cdot \sqrt{E_{calo}} \quad (5.15)$$

$$c(E_{calo}, \eta) = R_1(\eta) + R_2(\eta) \cdot E_{calo} - \frac{R_2(\eta)}{E_{calo}} \quad (5.16)$$

The point at 25 GeV has not been considered in the fit for the reason explained above; the extrapolation of the fit to these low energy produces good results, as it will be shown in next sections.

The energy dependence of a, b, c in this case is similar to the dependence obtained using the real presampler (see equations ??), which is another proof of the presampler capabilities of the S1 compartment. This dependence is more complicated than the one seen using variable X . On equivalent performance (it will be discussed in next chapter) variable X will be preferred for the correction of the energy lost in front for $\eta > 1.8$.

Also observed is the fact that there is an offset a different from zero, which means there can be energy loss in front but no energy detected in S1. This is

again interpreted as the absorption of very low energy photons and electrons present in the early shower.

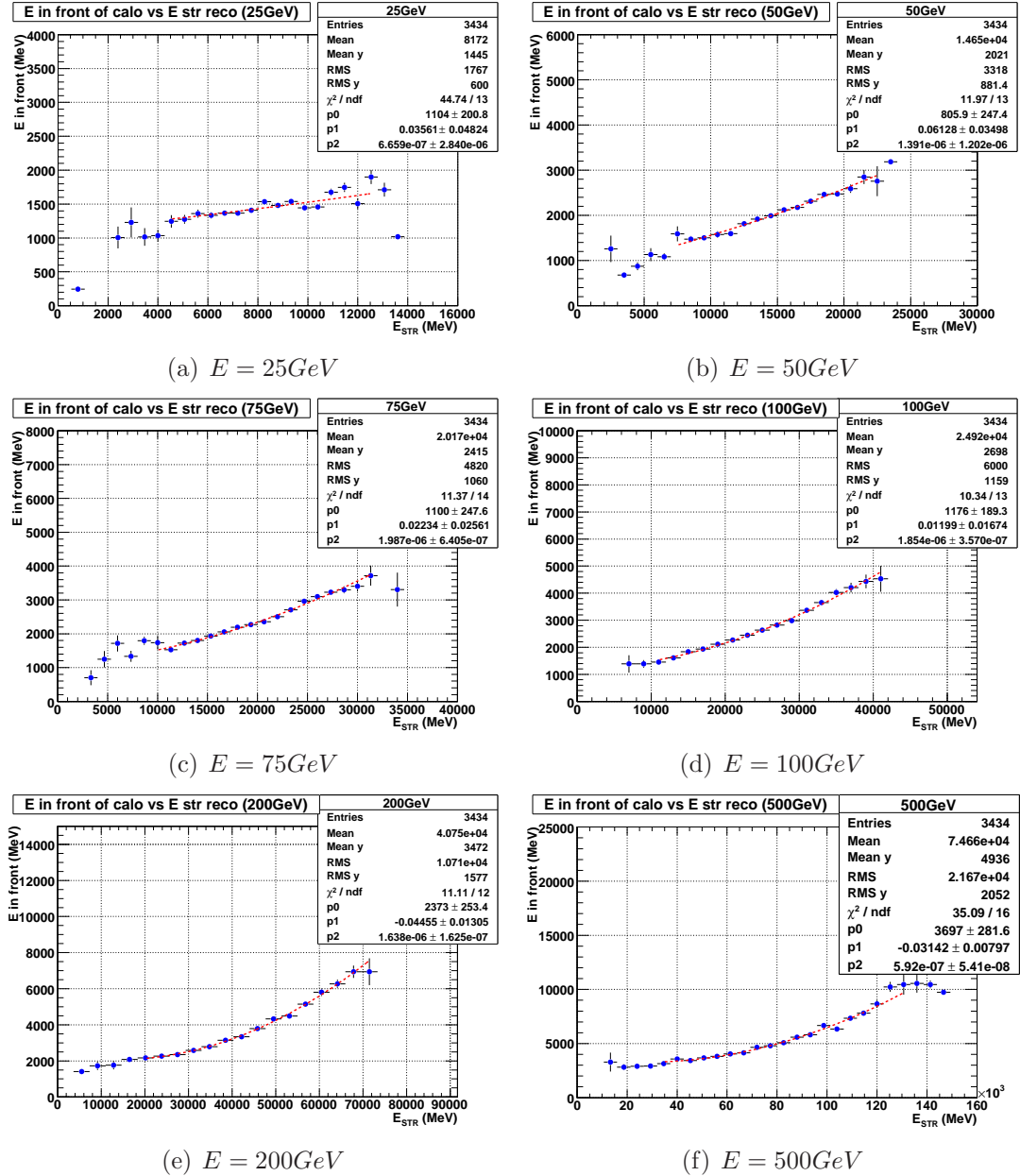


Figure 5.16: Energy in front of the calorimeter versus energy in the front sampling for different electron energies at $\eta = 1.9$

5.8 Summary

For the sake of clarity, the corrections of the Calibration Hits Method are summarized in table 5.1.

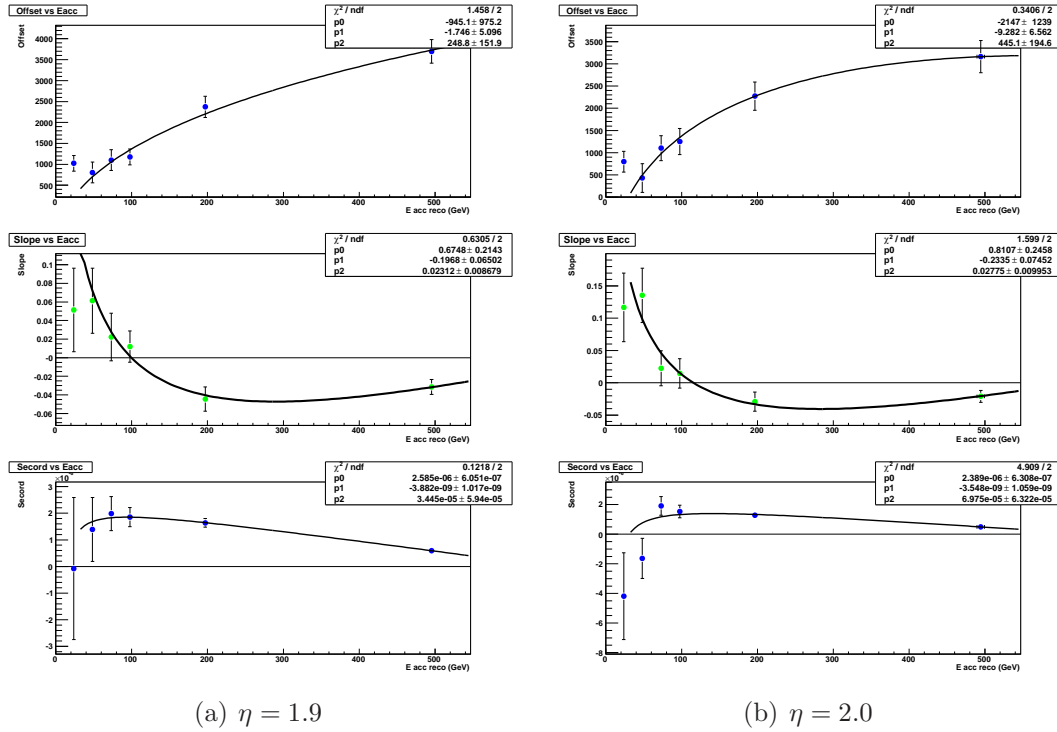


Figure 5.17: Parameters a, b, c of equation 5.13 as a function of E_{calo} . The left side column corresponds to $\eta = 1.9$, while the right side column corresponds to $\eta = 2.0$.

Correction	n_0 params/cluster	Cl dependence	total n_0 params
$E_{infront}$	9	no ($\times 1$)	9
E_{calo}	6	yes ($\times 3$)	18
E_{behind}	2	no ($\times 1$)	2
TOTAL	17		29

Table 5.1: Summary of the parameters used by the calibration hits method in each correction. The parameters corresponding to $E_{infront}$ refer a, b and c to equation 5.8 (equation 5.12 for $\eta > 1.8$). E_{calo} include the parameters of both f_{calo} (equation 5.3) and f_{out} (equation 5.5). Those parameters need to be computed for the three different cluster sizes. $E_{infront}$ includes the three parameters in equation 5.7.

Chapter 6

Results

The set of coefficients or parameters extracted in previous chapter are applied in Monte Carlo samples of single electrons to check the performance of the method in terms of energy resolution, linearity, uniformity and energy scale. The Monte Carlo samples differ from the ones used to obtain the parameters of the method. Some systematic errors are also studied in this chapter.

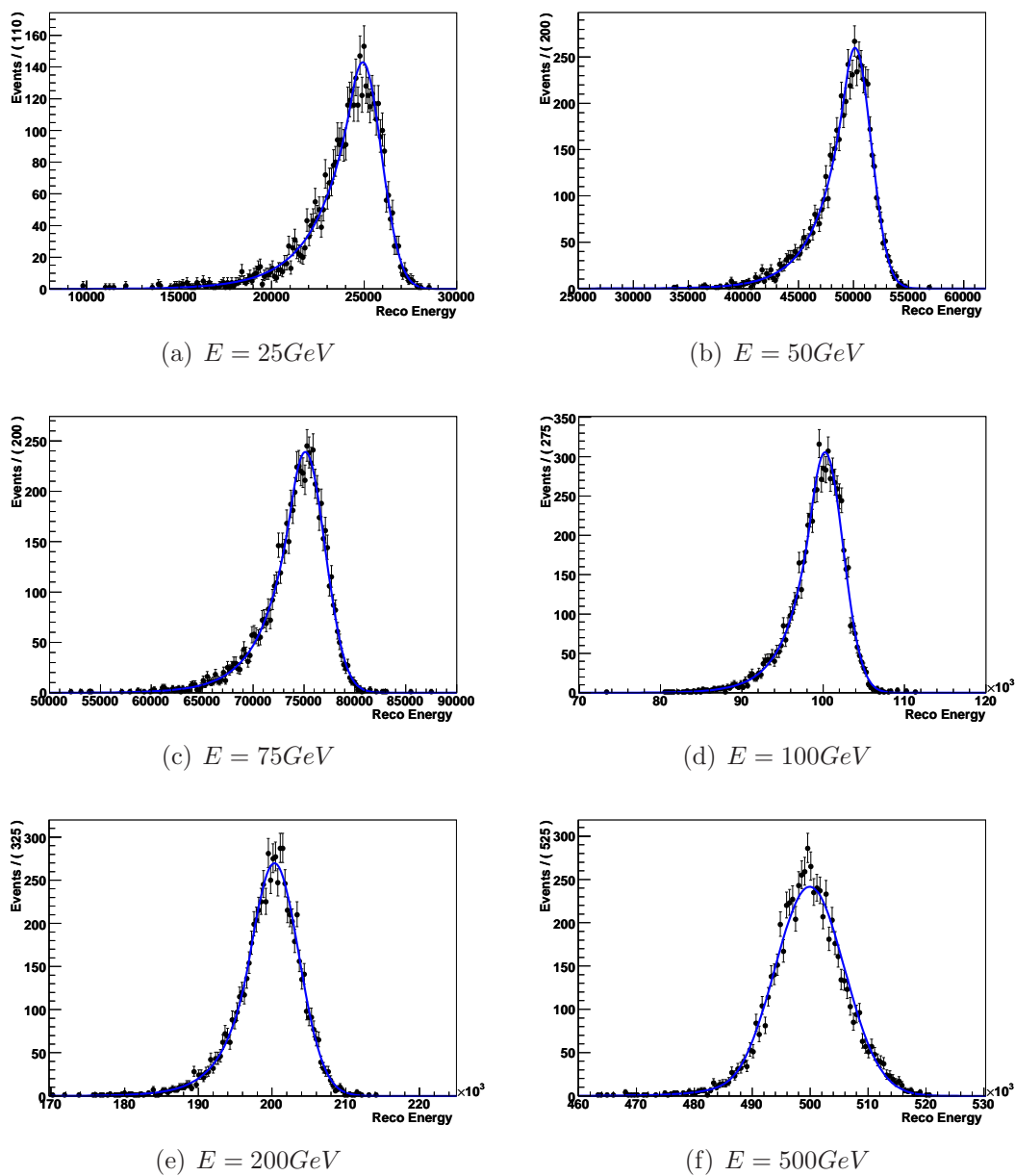
6.1 Energy resolution and linearity

The energy of the incoming electron is reconstructed using the procedure described in chapter 4, $E_{reco} = E_{infront} + E_{calo} + E_{behind}$, where the three different terms include the coefficients for the needed corrections. As an example, the distributions of E_{reco} are represented in figure 6.1 for different generated electron energies and for $\eta = 1.7125$. Under ideal conditions, perfect gaussian distributions for E_{reco} are expected. However, a low energy tail is observed at low generated energies. This is interpreted as the Calibration Hits Method (CHM), in the present release, is not able to correct totally the energy lost in front of the calorimeter. The influence of the dead material in front is less important for the highest energies, hence no tails are distinguished. The gaussian mean (m) and standard deviation (σ) are obtained from the gaussian part of the distribution by fitting the so called "Cristal Ball" function. It consists of a gaussian core portion and a power-law low-end tail below a certain threshold:

$$f(x) = \begin{cases} e^{-\frac{1}{2} \cdot \left(\frac{x-m}{\sigma}\right)^2} & \frac{x-m}{\sigma} > -|a| \\ \frac{\left(\frac{n}{|a|}\right)^n \cdot e^{-\frac{1}{2} \cdot a^2}}{\left(\frac{n}{|a|} - |a| - \frac{x-m}{\sigma}\right)^n} & \frac{x-m}{\sigma} \leq -|a| \end{cases}$$

6.1.1 Linearity

The average reconstructed energy (m) as a function of the generated electron energy is represented in figure (6.2) for two values of η , namely: 1.7125 (belongs to region with presampler) and 1.9125 (belongs to region without presampler). Apparently for

Figure 6.1: Reconstructed energies at $\eta = 1.7125$

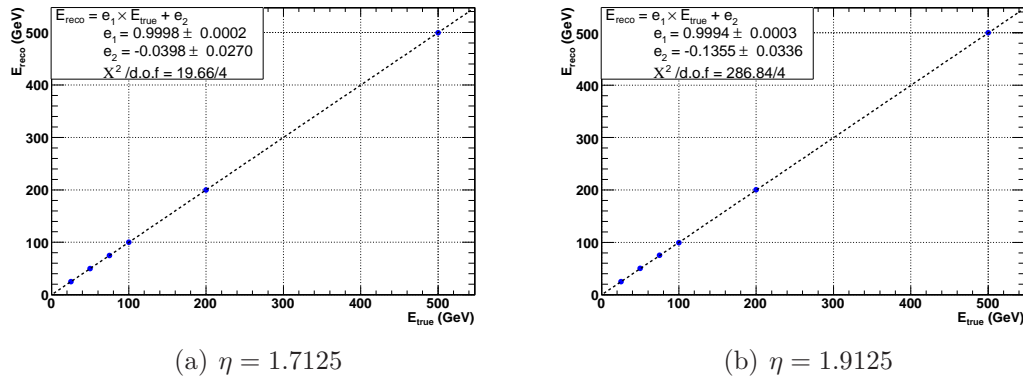


Figure 6.2: Reconstructed energy versus true energy superimposed with a first degree polinomial fit

both η values the relation is linear. However, to check the deviation from a linear relation at the per mil level, the points are fitted using a first degree polinomial and the following quantity is calculated for each point m_i , $i = 1, \dots, 6$:

$$\Delta m_i = \frac{m_i - E_{fit}}{E_{fit}}$$

where $E_{fit} = e_1 \cdot E_{true} + e_2$ being e_1 and e_2 the parameters of the fit.

The values of e_1 and e_2 are ($e_1 = 0.9998 \pm 0.0002$, $e_2 = -0.0398 \pm 0.0270$) for $\eta = 1.7125$ and ($e_1 = 0.9994 \pm 0.0003$, $e_2 = -0.1355 \pm 0.0336$) for $\eta = 1.9125$. The values of e_2 , represented as a funtion of η in figure 6.3 (a), are close to zero, but not compatible with this value. This fact indicates that the Calibration Hits Method is a little biased at very low energies. The values of e_1 (figura 6.3 b) are close to one, this parameter being related with the energy scale (E_{reco}/E) of the calorimeter.

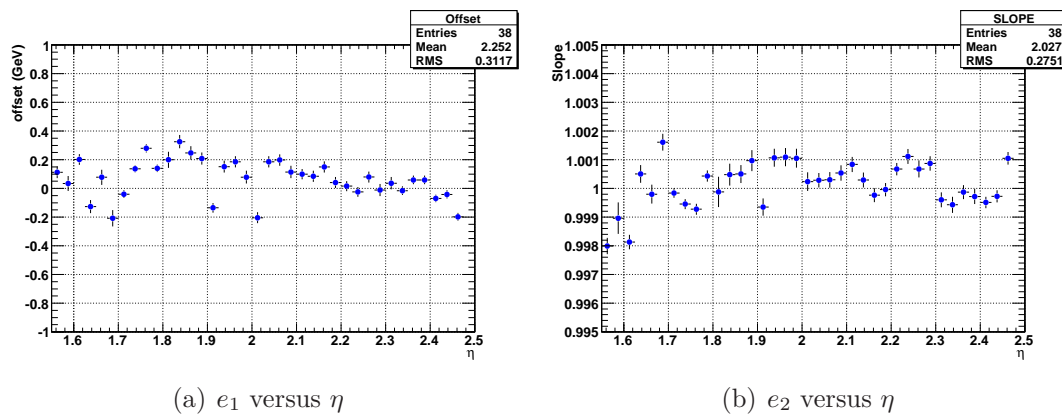


Figure 6.3: Uniformity of the parameters e_1 and e_2

In figure 6.4 the quantities Δm_i as a function of the generated electron energy (E) are shown. The left (right) raw correspond to $\eta = 1.7125$ ($\eta = 1.9125$). The energy lost in front of the calorimeter is corrected by using the parametrization function of

the shower barycenter X (see section 5.4.2), which is taken as default. At $\eta = 1.7125$ the deviation from linearity is below 0.1 % except for the point at 25 GeV, which is 0.5 %. At $\eta = 1.9125$ the linearity is worse being the low energy points at the level of 1%.

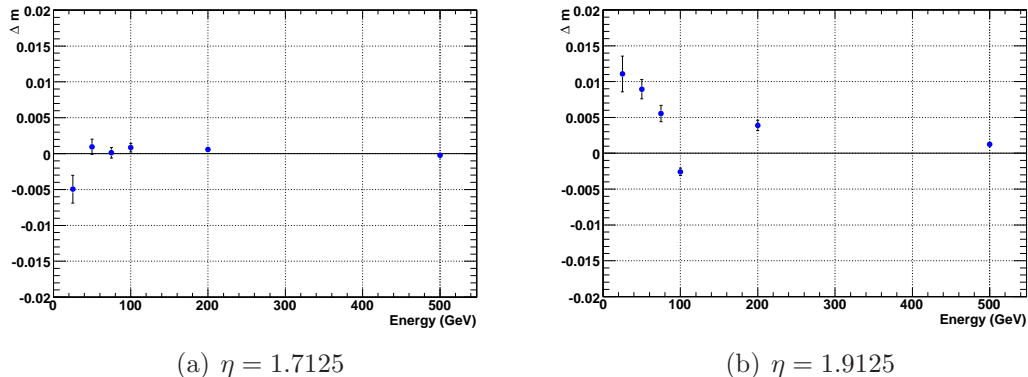


Figure 6.4: Δm versus energy

To study the uniformity of the linearity as a function of η , one quantity representing the deviation from linearity at a given pseudorapidity must be defined. One candidate is the maximum deviation from linearity defined as:

$$L = \Delta m_k$$

where k corresponds to the index which makes $|\Delta m_i|$ maximum.

This quantity L is shown as a function of η in figure (6.5). Except for three points, the rest are clearly below the 1% level.

6.1.2 Energy resolution

As seen in chapter 3 the energy resolution $\frac{\sigma}{m}$ is parameterized as:

$$\frac{\sigma(E)}{m(E)} = \frac{a}{\sqrt{E(\text{GeV})}} \oplus b \quad (6.1)$$

where a and b are the sampling and constant term respectively and \oplus means the quadratic sum.

A term c/E is not considered here since the Monte Carlo simulation, used in this study, does not include any noise.

In figure 6.6 the energy resolution as a function of the generated electron energy (E) is shown. The left (right) plot correspond to $\eta = 1.7125$ ($\eta = 1.9125$). The energy lost in front of the calorimeter is corrected by using the parameterization function of the shower barycenter X (see section 4.4.2), which is taken as default. The points are fitted using equation 6.1 obtaining the following values for the sampling and constant terms:

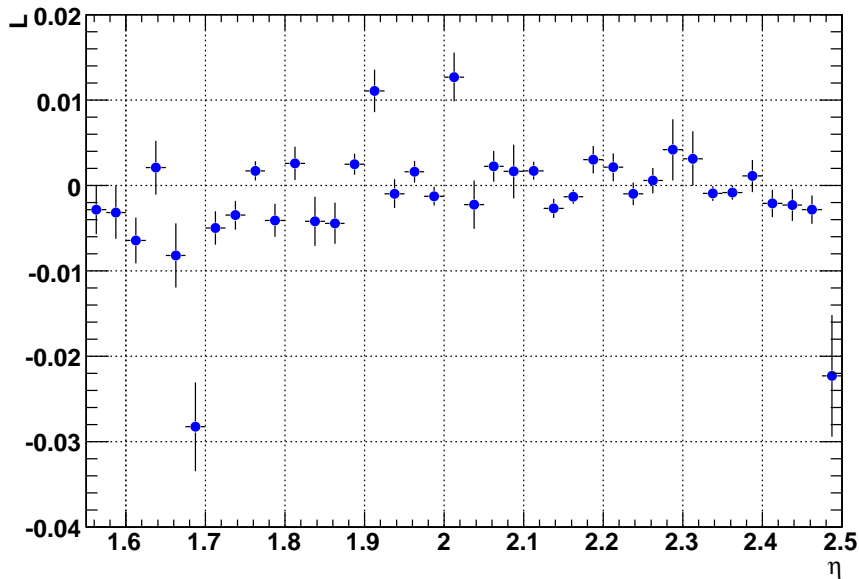
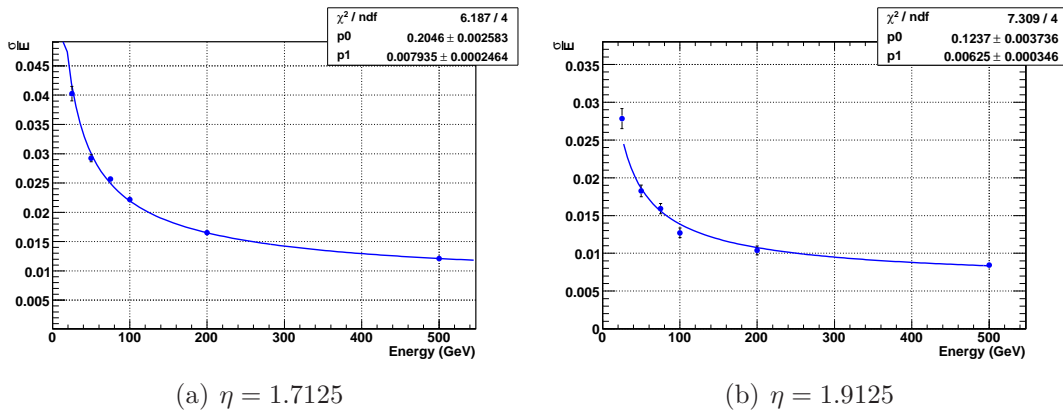
Figure 6.5: *Maximum deviation from linearity versus η .*

Figure 6.6: Resolution versus energy

$$a = 0.205 \quad b = 0.0079 \quad \eta = 1.7125$$

$$a = 0.124 \quad b = 0.0063 \quad \eta = 1.9125$$

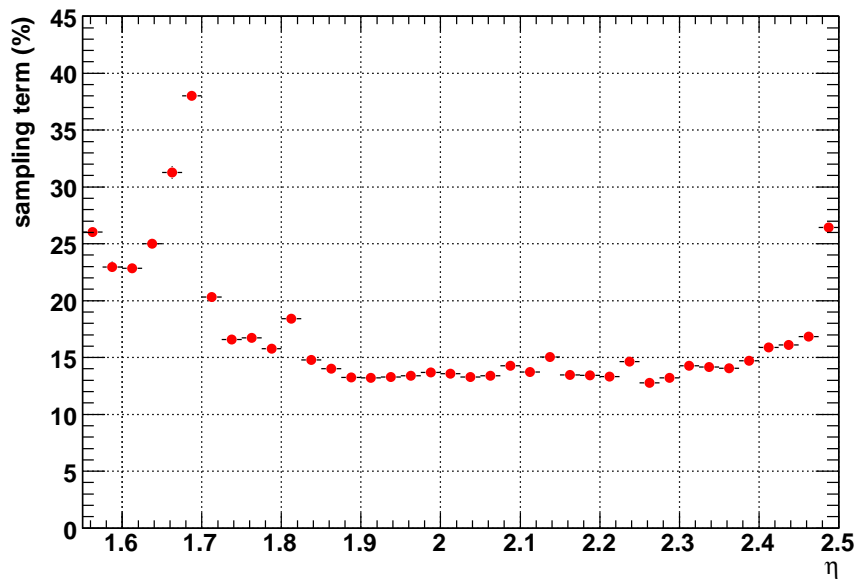
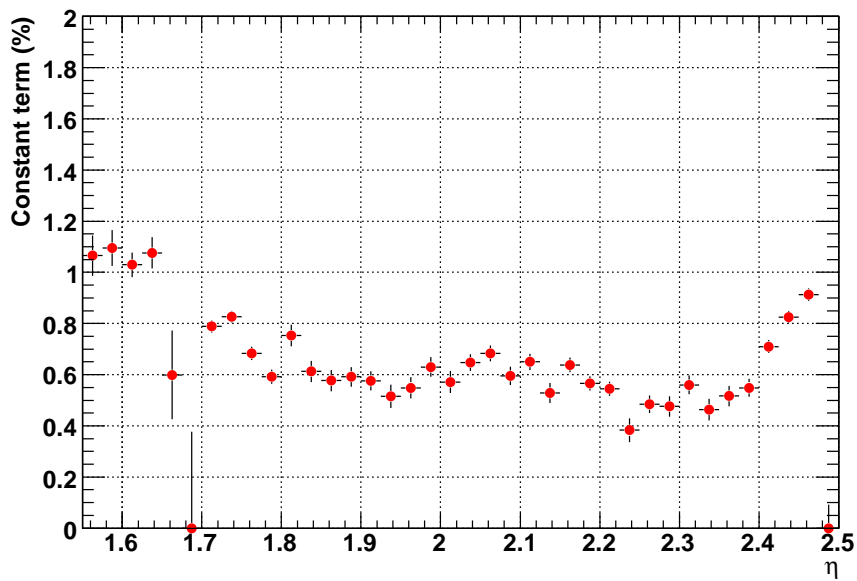
In the region around $\eta = 1.7$ the dead material in front has a higher value and larger variation than in the region about $\eta = 1.9$. This fact reflects on the different values obtained for the resolution, much better at $\eta = 1.9$. Again the present release of the Calibration Hits Method is not able to bring the sampling term to the level of 0.1 and the constant term to the level of 0.007 for the whole η region. To study the uniformity of the energy resolution the sampling and constant terms are represented as a function of η in figure (6.7). Both parameters show a flat behaviour in the η

range between 1.8 and 2.4 with values $a \sim 14\%$ and $b \sim 0.6\%$. However, there is a large variation on the sampling and constant term on the region $1.55 < \eta < 1.8$. The former varies from 16% up to 38% and the later from 0.6% up to 1.2%. This big variation, as we will discuss in the next section, is attributed to the huge variation of the amount of material in front of the calorimeter in this area. In fact it can be observed a correlation between the variation of the sampling term and the variation of the dead material in front represented in figure 4.9. The values of the constant term b for $\eta = 1.6625$ and $\eta = 1.6875$ are an artifice of the fit, namely for very high values of the sampling term there is less sensitivity to the constant term in the fit. In the region $\eta > 2.4$ both sampling and constant term increase again from 15% up to 20% and from 0.6% up to 1% respectively. This is probably due to the fact that in this η region no electron quality cuts (*isEM*) are applied to extract the coefficients due to low efficiency (see section "Description of the method" in previous chapter).

6.1.3 Uniformity of the response

The uniformity of the response along η is represented in figure 6.8 for both m and σ normalized to E . The normalization is performed to check the energy scale simultaneously. The achieved uniformity is better than 0.5% for all energies but 25GeV which goes up to 0.1% in several cells. This is due to the fact that low energy electrons are much more affected by energy loss in front of the calorimeter and by the effect of the magnetic field. The magnetic field reflects the charged particles of the pre-shower in the dead material, hence they missed the cluster of cells defined in the calorimeter to evaluate the energy (see f_{out} corrections in previous chapter).

Note also that an excellent energy reconstruction is achieved for electrons with energy higher than 100GeV being mostly within 0.3% in the whole η range. Finally we can see in figure 6.8b (also seen in figure 6.7) a small jump in the resolution at $\eta = 1.8$, which is the transition between the two regions with and without presampler. At this η cell the amount of material in front of the calorimeter is still big, as can be seen in figure 4.9, and the absence of the presampler produces a worst correction. This shows the advantage of having a presampler for recovering the energy lost in the material in front.

(a) Sampling term versus η (b) constant term versus η Figure 6.7: Resolution sampling and constant term over the whole η range

6.2 Contribution from the different corrections

First we would like to stress the necessity of applying a reconstruction method in order to improve the energy resolution, energy scale and linearity. With this goal we compare the energy scale and resolution, figures 6.9 and 6.10, when no corrections are applied at all (dark blue points), called raw energy in the graphic, with the case in

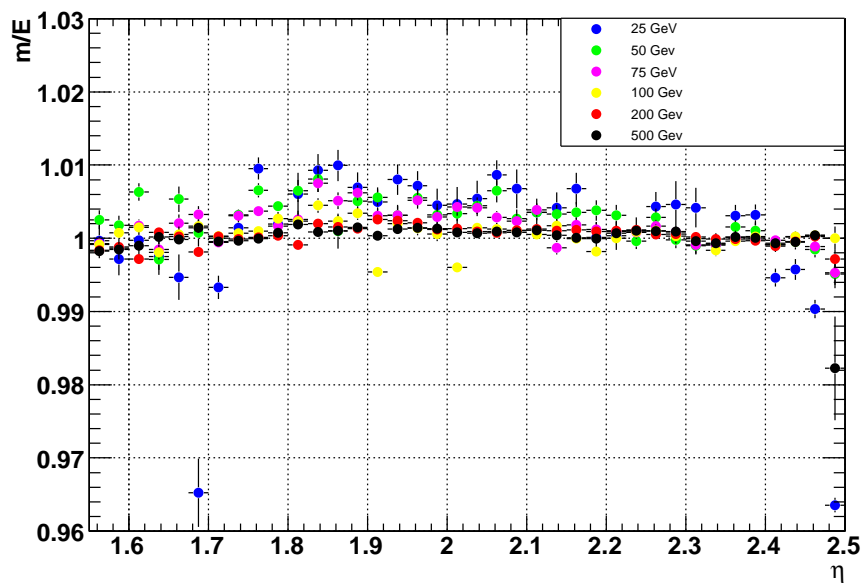
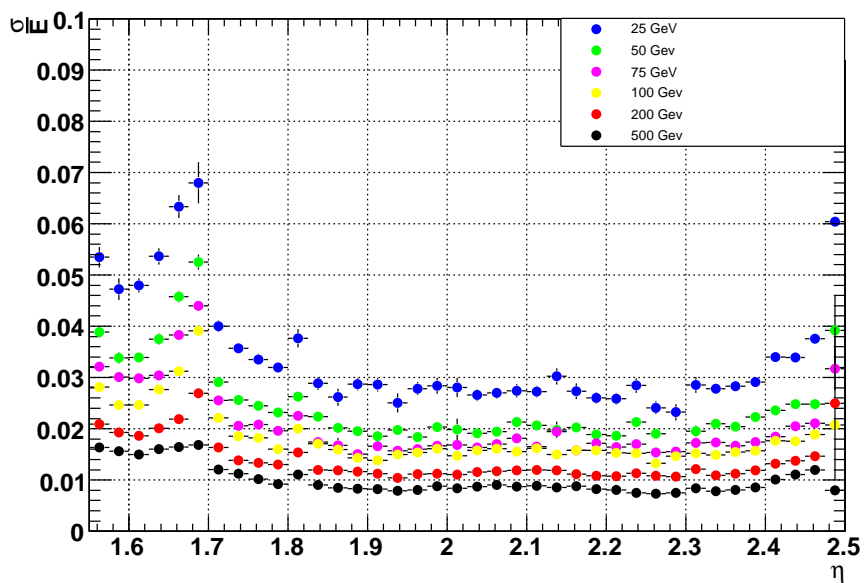
(a) Energy scale versus η (b) resolution versus η

Figure 6.8: Energy scale and resolution for the various energies versus eta. Blue, green, magenta, yellow, red and black points correspond to electrons of 25, 50, 75, 100, 200 and 500 GeV

which the Calibration Hits Method is used (green points). The left plots correspond to $\eta = 1.7125$ and the right ones to $\eta = 1.9125$. The abscissa refers to the generated electron energy (or true energy) E . It can be seen, for example, that at $\eta = 1.7125$

the raw energy is unacceptable, about 78% of the true 50 GeV, while applying the Calibration Hits Method to this raw energy leads to 99.999 % of the true energy. Similarly for the energy resolution one sees the improvement applying the Method at $\eta = 1.7125$. In contrast, at $\eta = 1.9125$ there is only improvement for the energy scale, but no gain for the resolution. In the region $\eta > 1.8$ the distribution of upstream material is flat and small so the corrections for energy in the calorimeter are expected to be the most important ones, and in particular the correction for lateral leakage. However this depends basically on the fluctuations of the transversal section of the electromagnetic shower that, as explained in chapter 3, is almost negligible.

As a second exercise, we discuss the contribution of the different corrections applied in the Calibration Hits Method to obtain the reconstructed energy. The modularity of the method allows to perform this kind of studies. Looking again at figures 6.9 and 6.10 and starting from the raw energy, the corrections are applied in an accumulative way following the order, f_{calo} (red points) thereafter f_{out} (cyan points), next is f_{leak} (yellow points) and last $f_{infront}$ (green points) which shows the performance of the full method.

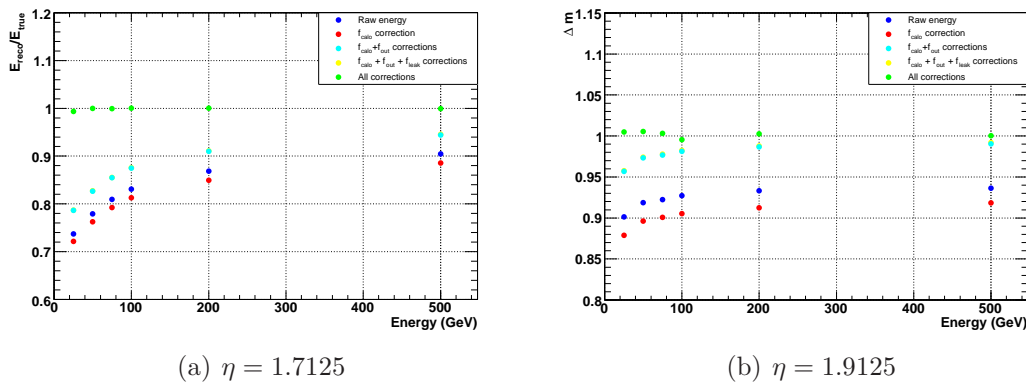


Figure 6.9: All different contributions to the Energy scale versus energy

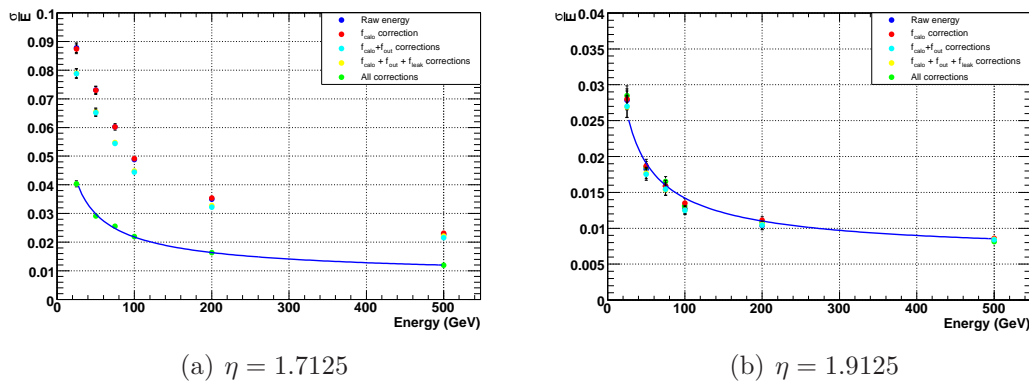


Figure 6.10: All different contributions to the resolution versus energy

The following exercise consists in fixing a certain generated energy, 100 GeV in

this case, and study the contribution of the different corrections as a function of η . This is represented in figure 6.11 for the energy scale and figure 6.12 for the resolution.

In the η interval (1.55, 1.8) the largest contribution to the energy scale as well as the resolution is the correction by energy loss in front of the calorimeter, improving the former up to 25% and the latter up to 55%. At η values above 1.8 that correction becomes less important, having an impact only on the energy scale of a few percent. The next significant correction is f_{out} , that is the correction for the cascade energy leaking transversally out of the defined cluster of calorimeter cells. It is hardly seen in the figures (light blue points) since the points are behind the yellow ones. It can be seen in figure 6.11 that the correction for the energy scale increases when η increases. This reflects the fact that the cell size in cm decreases when η increases, hence more lateral leakage is expected a larger η values. In addition to this effect, for the region $1.55 < \eta < 1.8$, where the dead material is higher, low energetic electrons from an early-cascade produced in the material are bent by the magnetic field, hence they may hit out of the calorimeter cluster.

The factor f_{calo} has the effect of correcting a small overestimation applied at the reconstruction level before the Calibration Hits Method. Finally, as expected, the contribution of the energy behind the calorimeter (f_{leak}) is almost zero since the fraction of energy deposited in this part of the detector never exceeds 1% of the total energy for very high energies and 0.2% for low energy electrons.

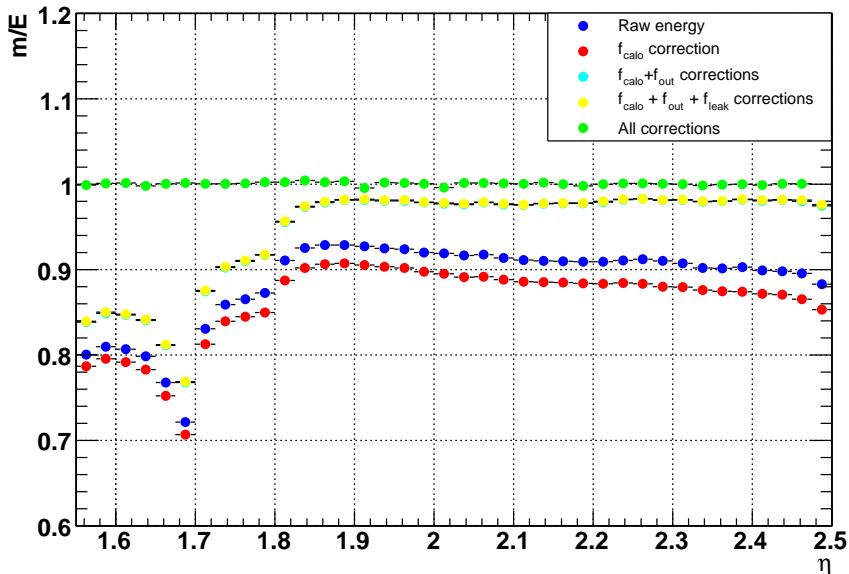


Figure 6.11: All different contributions to the energy scale (100 GeV) versus η .

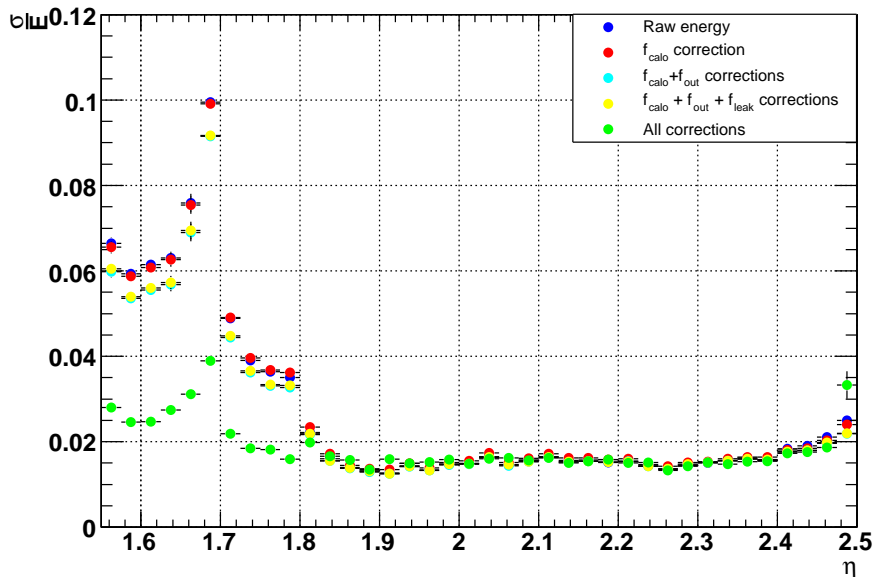


Figure 6.12: *Al* different contributions to the energy resolution (100GeV) versus η .

6.3 Systematics

In this section two sources of systematic errors for the energy reconstruction are studied, namely: i) cross talk between neighboring cells and ii) variations of the material in front with respect to the one implemented in the present release of the Monte Carlo simulation.

6.3.1 Effect of the cross talk

In several tests using charge injection and electron beams [13] it has been observed the existence of cross talk between cells. A calibration signal is injected in one individual cell and the neighborings are read out. Using this procedure it has been found that the highest cross talk is produced between strips of the S1 compartment ($S1 \rightarrow S1$ cross talk) reaching up to 5 %, in the η region where the S1-cells are smallest (see table 4.1 of η granularity). Cross talk was also observed from an S2 cell to the S1 and S3 compartments, $S2 \rightarrow S1$ and $S2 \rightarrow S3$ cross talks respectively, being in this case less than 1 %.

A first study of the cross talk effect on the CalibHits method has been done faking a cross talk not at the cell but at the cluster level, i.e., we moved a certain fraction of the energy of the cluster either from one compartment to another (so the total energy in the cluster remain constant) or from one compartment to outside the cluster. The former case has been used to fake $S2 \rightarrow S1$ as well as $S2 \rightarrow S3$ cross talks while the latter has been used to simulate energy underestimation due to $S1 \rightarrow S1$ cross talk.

Figure 6.13 (left) shows, at $\eta = 1.7125$, the effect of the $S2 \rightarrow S1$ cross talk on the computation of the barycenter of the shower, $\Delta X = X_{Xtalk} - X_{NoXtalk}$, as a

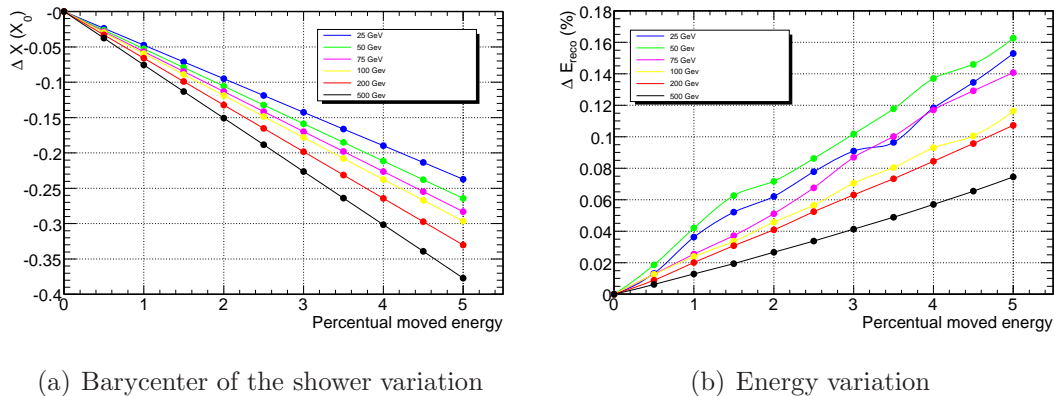


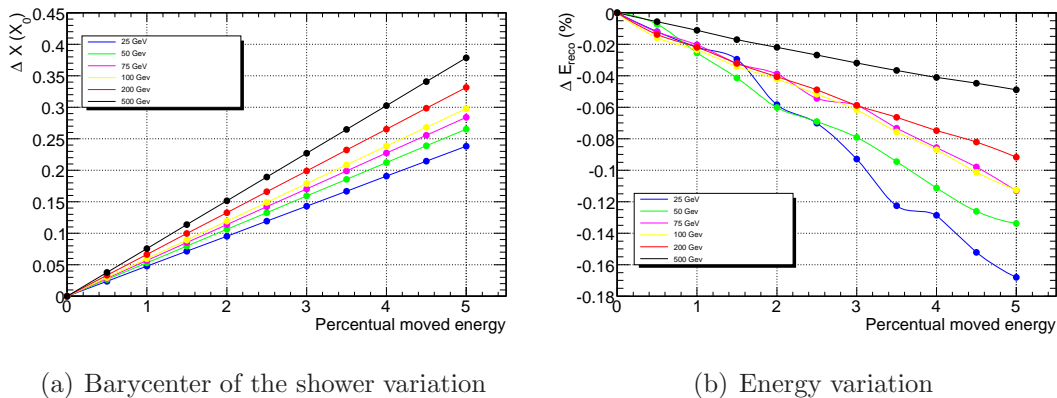
Figure 6.13: Effect of the Middle to Front cross talk at $\eta = 1.7125$

function of the percentual energy in the S2 sampling moved to the S1 compartment. Since part of the S2 energy is moved to S1, the value of X decreases, therefore ΔX is negative. It can be observed in the figure that for a 1 % cross talk, X drops 0.06 radiation lengths at 100GeV , which represents about 0.2 % of the total calorimeter depth.

In Figure 6.13 (right) it is represented, at $\eta = 1.7125$, the effect of the $S2 \rightarrow S1$ cross talk on the reconstructed energy, $\Delta E_{reco} = E_{reco}^{Xtalk} - E_{reco}^{NoXtalk}$, as a function of the percentual moved from S2 to S1. The reconstructed energy is modified by the $S2 \rightarrow S1$ due to its dependence on X . The term which dominates the energy variation is f_{out} , the correction for the energy leaked transversally out of the cluster. An underestimation of X produces an overestimation of the percentual energy out of the cluster (see figure 5.5), hence the reconstructed energy is overcorrected. For example, it can be observed in figure 6.13 that a $S2 \rightarrow S1$ cross talk of 1 % produces an increase in the reconstructed energy of about 0.02% at 100GeV . On the other hand, for low generated energies the longitudinal profile of the shower picks a lower X values (see equation 3.1), hence the underestimation of X is lower in percentage terms due to the non-linear behavior in figure 5.5, therefore a larger reconstructed energy variation is expected. This is also observed in figure 6.13 where the largest variation of the reconstructed energy corresponds to the lowest energy (25GeV). Even at 25GeV , a cross talk of 1% leads to a reconstructed energy variation of only 0.04 %, it is then a second order effect, hence we conclude that the $S2 \rightarrow S1$ cross talk does not affect the energy reconstruction.

Figure 6.14 shows the effect on X and E_{reco} of the $S2 \rightarrow S3$ cross talk at $\eta = 1.7125$. The same variables, ΔX and ΔE_{reco} are plotted but now the abscissa refers to the percentual energy moved from the S2 to the S3 compartment of the calorimeter.

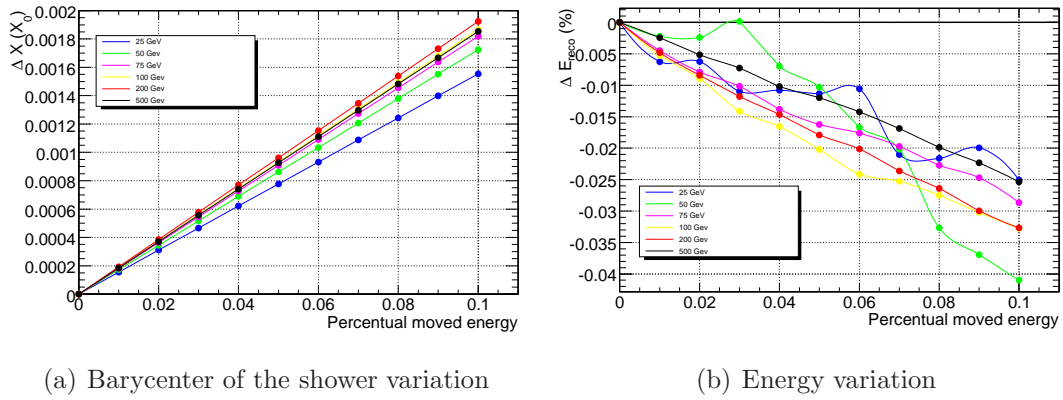
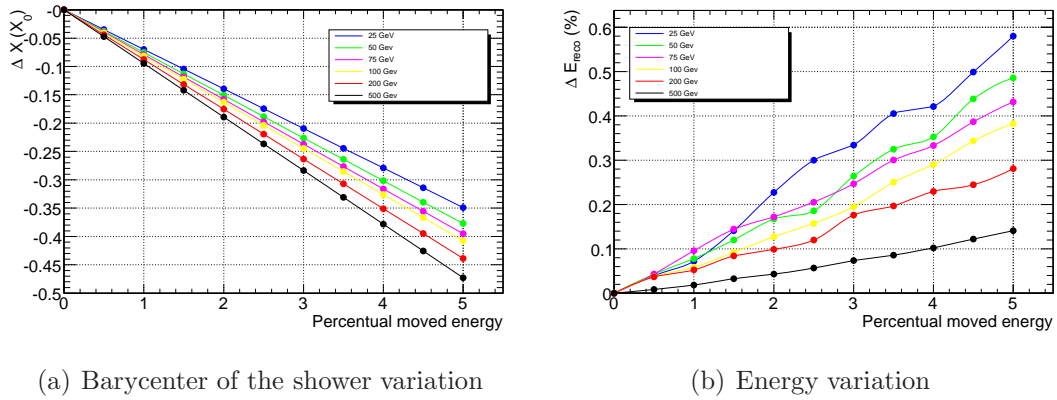
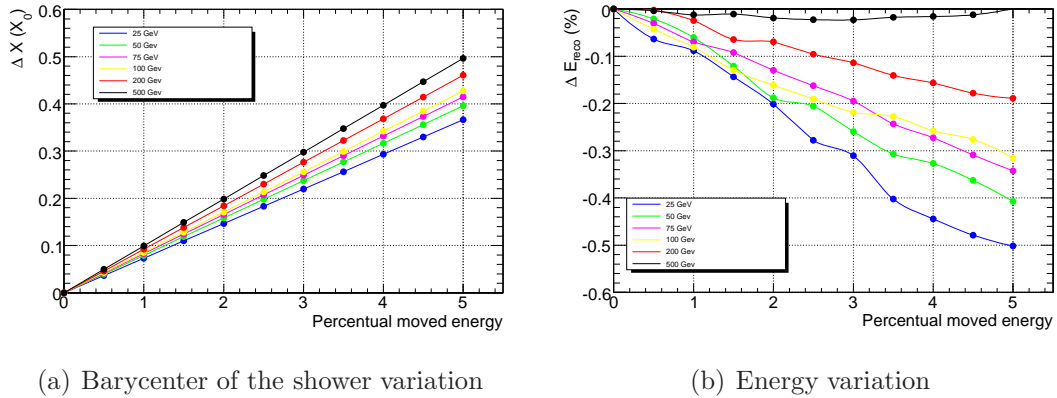
Again, the increase on ΔX is understood (figure 6.14 a) since we are moving a certain fraction of energy to the last compartement. In this case the correction for the energy leaked behind the calorimeter is potentially dangerous due to the exponential function used to parameterize f_{leak} (see figure 5.7). However, the large depth of the calorimeter in the whole pseudorapidity region produces that the extracted parameters l_0 and l_1 in (5.7) have a low value, being this f_{leak} insensitive to small

Figure 6.14: Effect of the Middle to back cross talk at $\eta = 1.7125$

variations of X . It is again the behaviour of f_{out} the one that dominates and with the above argument we understand the energy variations shown in (6.14 b). In this case the energy variation is on the opposite direction to the one produced by $S2 \rightarrow S1$ but affects quantitatively at the same level.

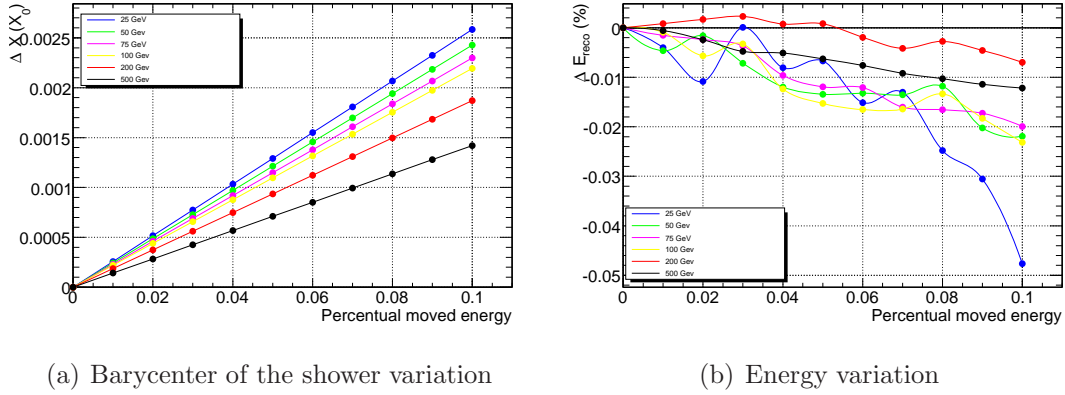
Finally, in figure (6.15) the results referring to the $S1 \rightarrow S1$ cross talk are presented. In contrast to previous types of cross talk, in $S1 \rightarrow S1$ part of the $S1$ energy is moved out of the cluster, hence the cluster energy is not conserved. This has two effects, first an increase of X , since E_1 is decreased respect to E_2 and E_3 , second a decrease of E_{reco} . The amount of cross talk, abscissas in the figure, has been established as follows: i) the cell to cell cross talk in $S1$ from measurements is at the level of 5%; ii) only the $S1$ -cell nearest to the cluster boundary will leak energy outside the cluster. The most negative situation will be a cluster 3×3 middle cells where the electron is incident on the edge of the central cell. The distance between the incident point of the electron and the boundary of the cluster is the width of one middle cell. According to the transverse profile of an electromagnetic shower at the depth of the $S1$ sampling, order 1% of the shower energy will be deposited in the $S1$ -cell nearest to the cluster boundary. This estimation has been obtained by transforming from Uranium to Lead the calculation of reference [5]. Then, the 5% cross talk of 1% Front energy is 0.05 % of E_1 to be moved out. This number must be considered as order of magnitude 0.1%, because of the rough calculation. It can be observed in figure 6.15 that, for instance at 100 GeV, a decrease of 0.1% in E_1 produces a reduction on E_{reco} of about 0.03%. The worst case being at 25 GeV were the variation of E_{reco} is 0.04%, hence, this cross also produces a negligible influence on the energy reconstruction.

For completeness, the same studies have been performed for the middle cell centered at $\eta = 1.9125$ in order to be sure that the different parameterizations used to compute the energy losses in the upstream material is not more sensitive to the cross talk. Figures 6.16, 6.17 and 6.18 show the effect of $S2 \rightarrow S1$, $S2 \rightarrow S3$ and $S1 \rightarrow S1$ cross talk respectively for the cell placed at $\eta = 1.9125$. Notice that the variations reach the same order of magnitude as in the cell centered at $\eta = 1.7125$.

Figure 6.15: Effect of the Front to Front cross talk at $\eta = 1.7125$ Figure 6.16: Effect of the Middle to Front cross talk at $\eta = 1.9125$ Figure 6.17: Effect of the Middle to back cross talk at $\eta = 1.9125$

6.3.2 Effect of an imperfect knowledge of the death material

The Calibration Hits method extract all the correction coefficients based on a Monte Carlo simulation, where the different properties of the ATLAS detector are implemented at a certain level of accuracy. In this subsection we try to quantify the

Figure 6.18: Effect of the Front to Front cross talk at $\eta = 1.9125$

possible deviation on the energy scale due to an imperfect knowledge of amount of materials in front of the Calorimeter.

As discussed in chapter 5, the only inputs to the CHM are the energies on the three samplings of the calorimeter plus the energy in the presampler. We have developed a new approach to estimate the effect on the energy reconstruction of an inaccurate knowledge of materials in front of the calorimeter.

In figure 6.19 the variation of the energy on the presampler and on the three layers of the calorimeter is shown as a function of the amount of material in front (M) for 100 GeV generated energy. The amount of material is expressed in units of radiation lengths (X_0). The points refer to the most probable value and the error bars to the RMS of the energy distributions. These dependences are obtained from the variation of the material in front along η organizing the Monte Carlo events in bins of M . We observe how the energy in the presampler is the most sensitive to this variation, changing its value up to a factor larger than 2 for $\sim 2 \cdot X_0$ of variation. The fitted functions in figures 6.19) are second degree polynomials: $E_i^{fit}(M)$, $i = 0, \dots, 3$, where the index 0 refers to presampler. These polynomials are used to estimate the energy depositions in a certain cell if the amount of material in front were different. The energy out of the cluster is included in the calculation of the total energy for the previous plots, hence the results are not biased by the possible differences in cell size along η . Similar functions are obtained for each generated energy point, finding that the parameters of the $E_i^{fit}(M)$ polynomials dependent on the energy.

The cluster energy in the different compartments is rescaled, using the polynomials $E_i^{fit}(M)$ for a certain variation of material in front respect to the nominal value, and the Calibration Hits Method (CHM) is applied under these different conditions (new values of E_0, E_1, E_2, E_3, E_4 for a given η). More explicitly, the rescaling is performed according to the following expression:

$$E_i^{new} = \frac{E_i^{fit}(M^{new})}{E_i^{fit}(M^{nominal})} E_i(M^{nominal}) \quad i = 0, 1, 2, 3$$

where $E_i(M^{nominal})$ is the cluster energy in compartment i for the nominal amount of material in front, and M^{new} refers to the new value for the amount of material.

With these new values E_i^{new} $i = 0, 1, 2, 3$, the barycenter X^{new} is computed and the new corresponding corrections (functions of X^{new} and E_i^{new}) of the CHM are applied to obtain E_{reco}^{new} .

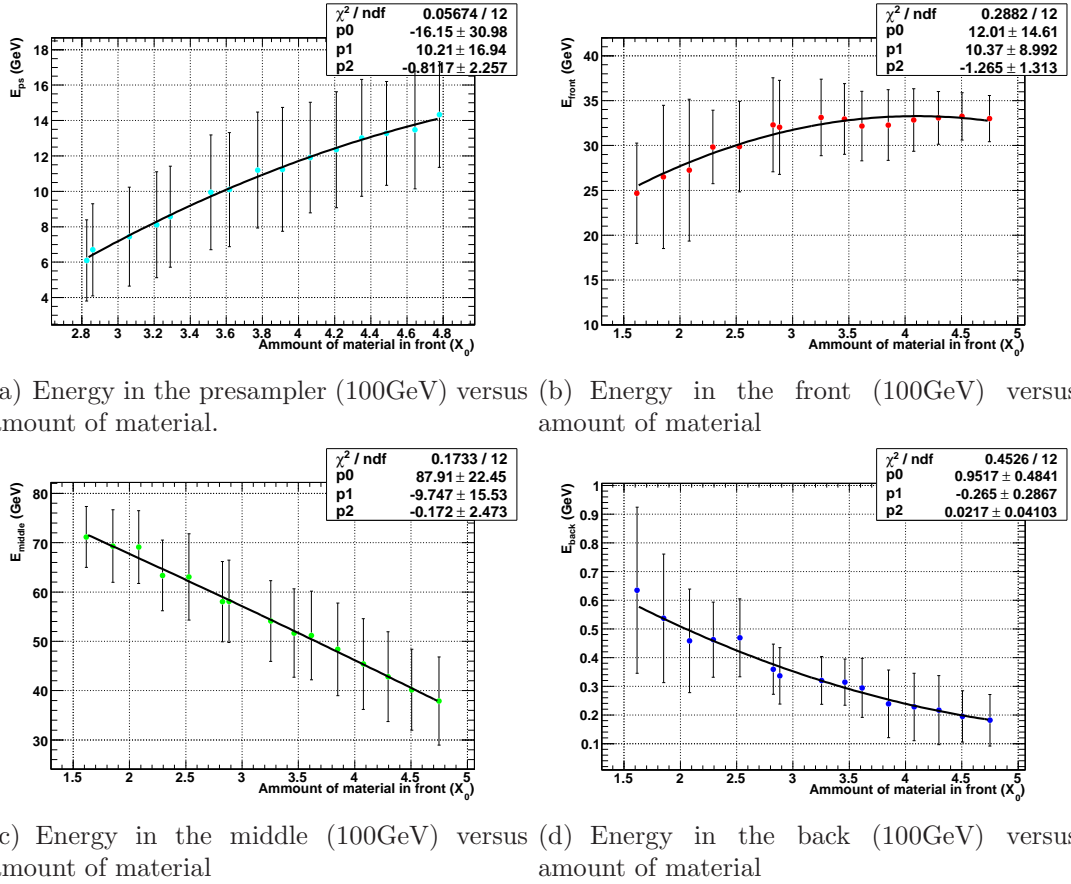
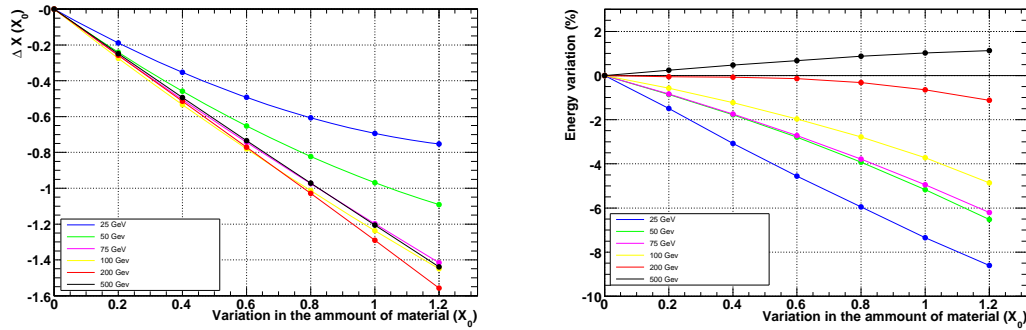


Figure 6.19: Effect of the variation of the amount of material in front in the Calorimeter on the energy deposited in the calorimeter

Figures 6.20(a),(b) show the variation of X^{new} and E_{reco}^{new} respectively with a change in the material in front respect to the nominal implementation. The figures refer to a position $\eta = 1.7125$, in the region equipped with presampler. The following definitions are used: $\Delta X = X^{new} - X^{nominal}$ and $\Delta E_{reco} = E_{reco}^{new} - E_{reco}^{nominal}$. The barycenter variation ΔX is negative, which means more contribution from the S1 compartment than for the S2,S3, and is less affected at low energies. More material in front means that the maximum of the electromagnetic shower moves occurs earlier, hence more energy in S1. The situation reminds the Middle to Front cross talk, figure 6.13, where part of the Middle compartment energy was moved to the S1 compartment. The effect on the reconstructed energy depends much on the generated energy being large, about 7% drop per X_0 material increase, at 25 GeV. We can also observe in figure 6.20 (b) that at 500 GeV the new extra material in front makes the reconstructed energy to increase. This is an effect of the correction functions in the CHM where different signs compete (see for instance figure 5.12 (b) for the parameters a,b,c of the $E_{in,front}$ correction). A similar reasoning can be made for the

region without presampler, as can be seen in figure 6.21 for $\eta = 1.9125$. However at this location the reconstructed energy is more affected by the variation of the amount of material in front, being about 16% drop per X_0 material increase. This may be explained by the fact that adding an extra X_0 of material in front means a larger relative increase at $\eta = 1.9$ than at $\eta = 1.7$.

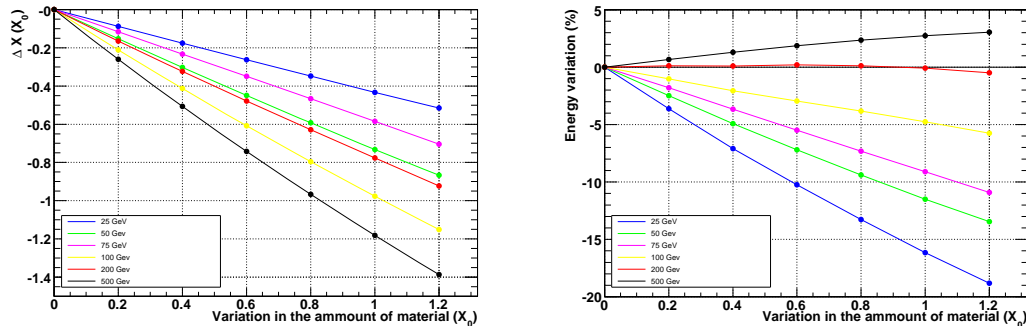
In conclusion, a fair knowledge of the material in front of the calorimeter is important to determine a precised reconstructed energy.



(a) Barycenter of the shower variation with the amount of material in front

(b) Effect of the material in front on E_{reco}

Figure 6.20: Effect of the variation of the amount of material in front on the reconstructed energy for electrons hitting at $\eta = 1.7125$



(a) Barycenter of the shower variation with the amount of material in front

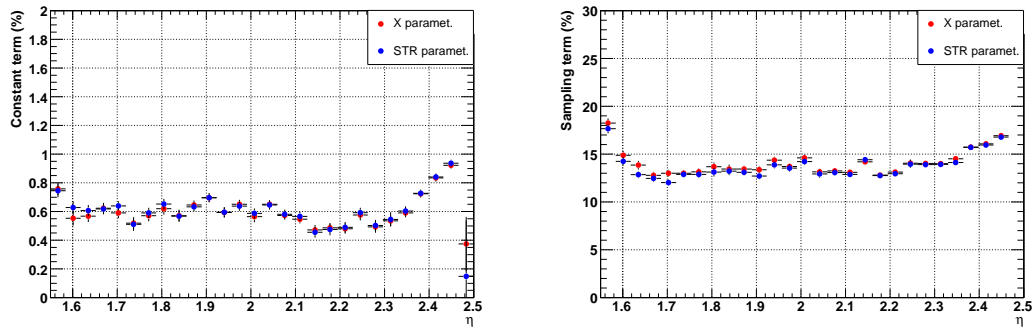
(b) Effect of the material in front on E_{reco}

Figure 6.21: Effect of the variation of the amount of material in front on the reconstructed energy for electrons hitting at $\eta = 1.9125$

6.4 Front method vs X method

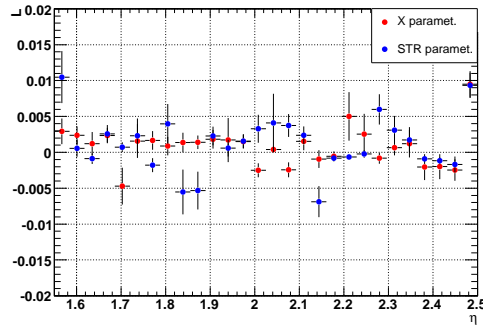
In section 5.7 two different approaches were considered to recover the energy lost in the material in front for $\eta > 1.8$, namely: i) the correlation of the energy loss with X (X method); ii) the correlation of the energy loss with E_1 (Front method). In the present section we compare both procedures in terms of energy resolution and linearity.

Figure 6.22 shows the constant term and sampling term (a , b respectively) of the energy resolution, as well as the linearity (c) as a function of η . The red points correspond to the Calibration Hits Method using the X method, while the blue points refer to the use of the Front method. Both methods give compatible results for the energy resolution, perhaps slightly more stable the X method than the Front method for the linearity.



(a) Resolution constant term versus η

(b) Resolution sampling term versus η



(c) Maximum deviation from linearity versus η

Figure 6.22: Comparison between the two possible methods in the region without presampler and resolution achieved with the strips method for the various energies.

Chapter 7

Conclusions

A new method to reconstruct the energy of electrons and photons, called Calibration Hits Method (CHM), applied sometime ago to the ATLAS Electromagnetic Barrel Calorimeter, has been adapted and tested with the Electromagnetic End-Cap Calorimeter. Some further developments to the method had to be done due to some peculiarities of the EMEC not present in the Barrel. The CHM corrects for the energy losses in material in front of the calorimeter as well as leakage, both transverse out of cell cluster definition and longitudinal behind the calorimeter.

To obtain these energy losses a special Monte Carlo simulation of the ATLAS response to single electron has been run, where the electrons are produced at the nominal interaction point with 6 different energies ranging from 25 to 500 GeV. The simulation included the nominal ATLAS geometry, taking into account the effect of the magnetic field as well as the vertex spread at the interaction point.

The 17 parameters of the CHM are obtained as functions of measurable quantities, namely: the energy in presampler, front, middle and back calorimeter compartments and the pseudorapidity (η) of the electron impact point. Corrections are applied at the cell cluster level, i.e. to the cluster energy, where several cluster sizes have been studied.

The energy reconstructed using this CHM method is checked in terms of linearity and energy resolution. For the region $\eta > 1.8$ the deviation from linearity is better than 0.5%, except for two points that need to be understood, while the sampling and constant terms of the energy resolution are $a \sim 14\%$ and $b \sim 0.6\%$ respectively. In the region $1.55 < \eta < 1.8$, more affected by the material in front of the calorimeter, the linearity has been found better than 1% and the sampling and constant terms of the energy resolution in the intervals $a \sim 15 - 35\%$ and $b \sim 0.5 - 1\%$. The method needs further developments to improve the results in the latter region.

Some sources of systematic errors have been studied, namely i) the influence of the cell to cell cross talk, and ii) the effect of an inaccurate knowledge of the material in front of the calorimeter. The former is not a concern for the energy reconstruction using the CHM, while the latter may introduce variations at the level of 10% per X_0 of material increase for low energies (25 GeV).

Bibliography

- [1] *The ATLAS Experiment at the CERN Large Hadron Collider*; ATLAS Collaboration; ATL-COM-PHYS-2007-087.
- [2] Liquid Argon Calorimeter TDR, CERN/LHCC/96-41
- [3] U. Amaldi, "*Fluctuations in Calorimetry Measurements*", *Physica Scripta*, Vol. 23 pp.409-424 (1981).
- [4] C. Fabjan, "*Experimental techniques in High Energy Physics*". CERN, Geneva, 1985. CERN-EP/85-84.
- [5] *Fast Simulation of Electromagnetic Showers in the ZEUS Calorimeter*; J. del Peso, E. Ros; Nucl.Instrum.Meth.A306:485-499,1991
- [6] L. Landau, J. Phys. USSR 8, 201 (1944).
- [7] *On the Energy Resolution of Electromagnetic Sampling Calorimeters*; J. del Peso, E. Ros; Nucl.Instrum.Meth.A276:456,1989
- [8] C. Fabjan, "*Calorimetry in High Energy Physics*", *Techniques and Concepts of High Energy Physics-III*, T. Ferbel, ed. Plenum Pub. Corp., 1985.
- [9] B. Aubert et al.; *Performance of the ATLAS electromagnetic calorimeter endcap module 0*; Nucl.Inst.Meth. A500(2003)178.
- [10] F. Hubaut, C. Serfon *Response Uniformity of the Atlas electromagnetic endcap calorimeter* atlas-larg-pub-2004-015
- [11] C. Oliver, J. del Peso *Outer Wheel Uniformity of the ElectroMagnetic Endcap Calorimeter* atlas-larg-pub-2005-002
- [12] Calibration of the ATLAS electromagnetic calorimeter using calibration hits; D. Banfi, L. Carminati, L. Mandelli; larg-pub-2007-012
- [13] J. Colas, C. La Taille, R. Lafaye, N. Massol, P. Pralavorio, D. Sauvage, L. Serin *Crosstalk in the ATLAS Electromagnetic Calorimeter* atlas-larg-2004-004
- [14] W. Verkerke, D. Kirkby *RooFit User Manual V2.07* Document Version 2.07.29, 11 January 2006